OPEN ACCESS
IOP Publishing
Journal of Physics: Condensed Matter
J. Phys.: Condens. Matter **36** (2024) 273001 (28pp)
https://doi.org/10.1088/1361-648X/ad3603

Topical Review

Recent progress on topological semimetal IrO_2: electronic structures, synthesis, and transport properties

T X Zhang[1], A L Coughlin[1], Chi-Ken Lu[2], J J Heremans[3] and S X Zhang[1,4,*]

[1] Department of Physics, Indiana University, Bloomington, IN 47405, United States of America
[2] Department of Mathematics and Computer Science, Rutgers University, Newark, NJ 07102, United States of America
[3] Department of Physics, Virginia Tech, Blacksburg, VA 24061, United States of America
[4] Quantum Science and Engineering Center, Indiana University, Bloomington, IN 47405, United States of America

E-mail: sxzhang@indiana.edu, cl1178@rutgers.edu and heremans@vt.edu

Received 1 December 2023, revised 24 February 2024
Accepted for publication 20 March 2024
Published 10 April 2024

Abstract

5*d* transition metal oxides, such as iridates, have attracted significant interest in condensed matter physics throughout the past decade owing to their fascinating physical properties that arise from intrinsically strong spin-orbit coupling (SOC) and its interplay with other interactions of comparable energy scales. Among the rich family of iridates, iridium dioxide (IrO_2), a simple binary compound long known as a promising catalyst for water splitting, has recently been demonstrated to possess novel topological states and exotic transport properties. The strong SOC and the nonsymmorphic symmetry that IrO_2 possesses introduce symmetry-protected Dirac nodal lines (DNLs) within its band structure as well as a large spin Hall effect in the transport. Here, we review recent advances pertaining to the study of this unique SOC oxide, with an emphasis on the understanding of the topological electronic structures, syntheses of high crystalline quality nanostructures, and experimental measurements of its fundamental transport properties. In particular, the theoretical origin of the presence of the fourfold degenerate DNLs in band structure and its implications in the angle-resolved photoemission spectroscopy measurement and in the spin Hall effect are discussed. We further introduce a variety of synthesis techniques to achieve IrO_2 nanostructures, such as epitaxial thin films and single crystalline nanowires, with the goal of understanding the roles that each key parameter plays in the growth process. Finally, we review the electrical, spin, and thermal transport studies. The transport properties under variable temperatures and magnetic fields reveal themselves to be uniquely sensitive and modifiable by strain, dimensionality (bulk, thin film,

* Author to whom any correspondence should be addressed.

nanowire), quantum confinement, film texture, and disorder. The sensitivity, stemming from the competing energy scales of SOC, disorder, and other interactions, enables the creation of a variety of intriguing quantum states of matter.

Keywords: 5*d* transition metal oxides, iridium dioxide, spin-orbit coupling, Dirac nodal line semimetal, spin Hall effect, thermal transport

1. Introduction

3d transition metal oxides (TMOs), such as manganites and cuprates, have fascinated condensed matter physicists for many decades due to their intriguing physical properties, including Mott insulator states [1–3], unconventional superconductivity [4–7], colossal magnetoresistance [8–11], magnetoelectric effects [12–14], and beyond. These remarkable electronic and magnetic properties originate from the strong Coulomb interactions between the 3*d* electrons which occupy the compact orbitals of the transition metals [15, 16]. Moving downwards in the periodic table from *3d* to *4d* and to *5d*, the electron interaction U decreases as the partially filled d orbitals become more spatially extended; on the other hand, spin-orbit coupling (SOC or λ), a key ingredient for topologically non-trivial states [17–19], increases dramatically as the atomic number increases and becomes comparable with the U and other energy scales (e.g. crystal field Δ) in 5*d* TMOs [20, 21]. The interplay and competition between SOC, U, Hund's coupling, and Δ foster the emergence of novel topological quantum phases [22–24], such as spin-orbit-assisted Mott insulators [25, 26], topological Mott insulators [27], magnetic Weyl semimetals [28, 29], axion insulators [28, 30], quantum spin liquids [31–34], etc. Compared to many other non-oxide topological materials in which the non-interacting *s* or *p* electrons play key roles, TMOs of 5*d* electrons host correlated topological states where correlation and topology are intricately twined, leading to strong couplings between the spin, lattice, orbital and charge degrees of freedom. Furthermore, unlike many of the non-oxides such as selenides or tellurides which are air-sensitive [35–37], topological oxides are chemically stable in air, offering a technological advantage for future topological device applications.

The most well-studied 5*d* TMOs in recent years are the family of iridium oxides (or iridates). In this topic review, we focus on the simplest binary iridate compound, namely iridium dioxide (IrO_2), which has been long known as a promising electrocatalyst for oxygen evolution reactions [38–41]. As shown in figure 1(a), IrO_2 has a rutile tetragonal crystal structure with lattice parameters $a = b = 4.498$ Å, $c = 3.154$ Å and belongs to the space group P42/mnm [42]. Like in many other iridates, each Ir atom in the rutile lattice is coordinated with six oxygen atoms which form a (distorted) IrO_6 octahedron. In a *perfect* octahedral crystal field (without distortion), the 5*d* orbitals are split into an e_g doublet and a t_{2g} triplet, and the latter can be regarded effectively as an $L = 1$ state. The SOC further entangles the orbital and the spin degrees of freedom, forming a doublet $J_{\text{eff}} = 1/2$ and a quartet $J_{\text{eff}} = 3/2$ [25]. Since the Ir^{4+} ion contains five 5*d* electrons, the $J_{\text{eff}} = 3/2$ states at a lower energy are completely filled, whereas the $J_{\text{eff}} = 1/2$ states around the Fermi level are partially occupied (figure 1(b)) [25, 26]. While the $J_{\text{eff}} = 1/2$ state has been demonstrated to be a novel ground state in many insulating iridates (e.g. Sr_2IrO_4), recent hard x-ray photoelectron spectroscopy and x-ray absorption (XAS) spectroscopy studies suggest that this widely accepted model may not be applicable in metallic IrO_2 where the distortion of the octahedron lifts the degeneracy of the t_{2g} triplet [43, 44].

Furthermore, unlike many other iridates (e.g. pyrochlore, Ruddlesden–Popper, and perovskite iridates) where the IrO_6 octahedra are connected in a corner-sharing-only network, the octahedra in the rutile lattice share not only corners but also edges with their neighbors (figure 1(c)) [45]. This strong octahedral connectivity facilitates the hopping of electrons (t), yielding a weak effective electron–electron interaction ratio (U/t) and hence a nearly uncorrelated metallic behavior in the system. Despite the relatively weak electron interactions, the nonsymmorphic symmetry in IrO_2 gives rise to a rich band structure which is characterized by several band touching points and lines in the three-dimensional (3D) momentum space [46–50]. Interestingly, the strong SOC can partially lift the band degeneracy, promoting a spin Hall transport associated with the spin-momentum entangled electronic states [48, 51–54]. The exotic topological manifestations and intriguing transport properties have made this simple binary compound one of the most attractive iridates for both fundamental research and technological advances.

In this topic review, we first introduce the topological electronic band structures of IrO_2, with a focus on the role that the nonsymmorphic symmetry plays on the presence of Dirac nodal lines (DNLs) in the band structure, the gap opening due to SOC, the Fermi surfaces observed in angle-resolved photoemission spectroscopy (ARPES), and a discussion of how this leads to the observed spin Hall effect. We then provide a survey and discussion of various techniques for the synthesis of IrO_2 thin films and nanostructures, and finally a detailed review of their electrical, spin, and thermal transport properties. Since we attempt to focus on the fundamental condensed matter and materials physics, the electrochemical-related properties of IrO_2 and its potential applications in electrocatalysis, electrochromic devices, chemical sensors, etc are not discussed. There are several recent review articles in these areas [55–59] that we encourage the readers to consult.

2. Electronic structures

In this section, we review the electronic structure of IrO_2. Specifically, we focus on a discussion of the $J_{\text{eff}} = 1/2$ model,

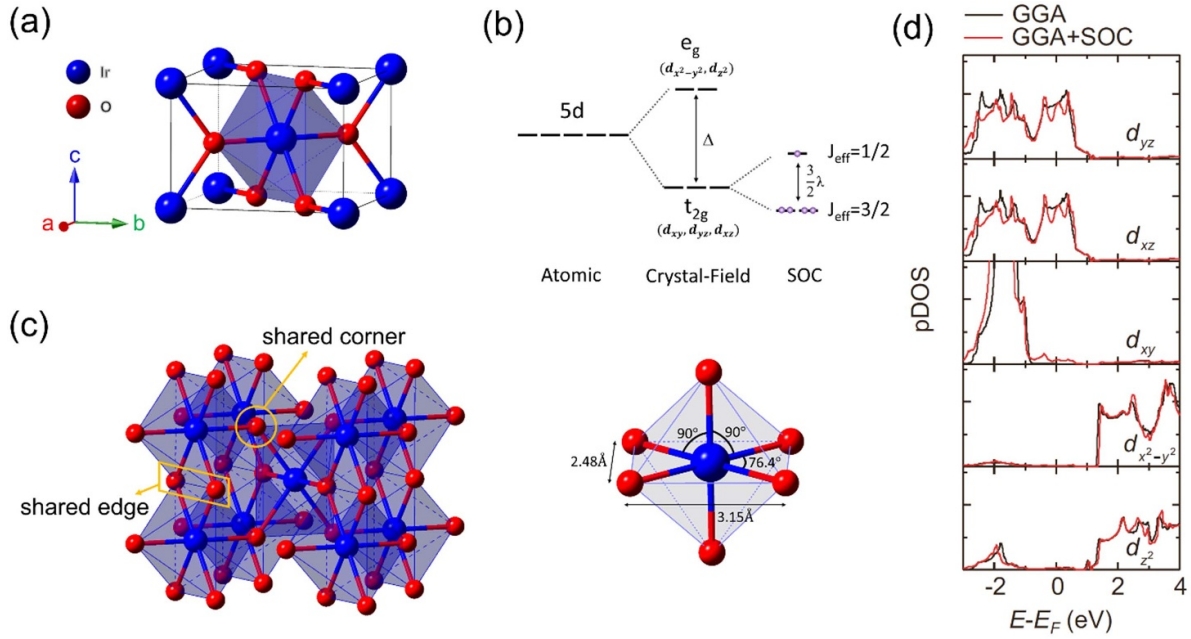

Figure 1. (a) Rutile crystal structure of IrO_2. (b) Upper panel: a generic $J_{\text{eff}} = 1/2$ model describing the splitting of 5*d* states by a perfect octahedral crystal field and strong SOC; bottom panel: a schematic illustrating the distortion of an IrO_6 octahedron; (c) IrO_6 octahedra with shared corners and edges in IrO_2. (d) Projected density of states of the three t_{2g} orbitals and two e_g orbitals in IrO_2. Reprinted (figure) with permission from [44], Copyright (2016) by the American Physical Society.

the origin of the DNLs in the presence of strong SOC and non-symmorphic symmetry, and their relevance to the observed spin Hall effects.

2.1. Possible breaking down of the $J_{\text{eff}} = 1/2$ model

In iridates, the iridium ion inside the IrO_6 octahedron has five valence electrons occupying the *d*-orbitals. A well-accepted picture which considers the effects of the crystal field and SOC is the ground state with a half-filled $J_{\text{eff}} = 1/2$ and a filled $J_{\text{eff}} = 3/2$ [25, 26]. The $J_{\text{eff}} = 1/2$ picture applies to many of the insulating iridates (e.g. Sr_2IrO_4) [60–62] where the valence band width near the Fermi level is reduced by the SOC and a moderate U is sufficient to localize the electron in $J_{\text{eff}} = 1/2$. In IrO_2, optical conductivity measurements show a Drude-like response, confirming the presence of free electrons [44, 63]. While earlier resonant x-ray scattering measurements revealed the possible existence of the $J_{\text{eff}} = 1/2$ state in IrO_2 [64], more recent polarization-dependent XAS spectroscopy studies suggest the absence of such ground state [44]. An important ingredient for the formation of $J_{\text{eff}} = 1/2$ is the degeneracy among three t_{2g} orbitals in the presence of crystal field and hybridization with neighboring oxygen orbitals. Density functional theory (DFT) calculations [43, 44, 65, 66] show that while the *xz* and *yz* orbitals are still degenerate near the Fermi level, the *xy* orbital is pushed down by around 2 eV (figure 1(d)). This observation is not compatible with the $J_{\text{eff}} = 1/2$ wave functions in which all three orbitals shall contribute to the density of states equally [43, 44]. The energy separation between *xy* and the other two t_{2g} orbitals is attributed to the different bonding symmetries with the neighboring oxygen orbitals [43, 44]. This conjecture was supported by the polarization-dependent XAS measurement in which the π-polarization absorption is greatly suppressed in comparison with the σ-polarization one [44]. In spite of the debate on $J_{\text{eff}} = 1/2$ states [20, 21, 43, 44, 64], it is widely accepted that SOC plays a vital role in the electronic structure of IrO_2, as discussed below.

2.2. Role of electron interaction and SOC

Photoemission spectroscopy studies [45, 67, 68] in correlation with DFT calculations [69] have suggested that the electron correlation is rather weak in IrO_2, due to the high connectivity of the IrO_6 octahedra in the rutile structure [45]. As a result, the electron–electron interaction is not included in most DFT calculations of the electronic band structure [48, 50, 70, 71]. Although the band structure calculations in earlier years did not consider SOC either [70, 72, 73], recent studies highlight its essential role in determining the electronic properties of IrO_2 [20, 63, 64, 68]. A representative band structure along the high symmetry axes is shown in figures 2(a) and (b), where the effect of SOC was studied [71]. From $X = (\pi, 0, 0)$ to $M = (\pi, \pi, 0)$, DNLs with four-fold degeneracy appear near the Fermi level ($E = 0$) regardless of the SOC. Nevertheless, SOC has a strong influence on the bands along $A = (\pi, \pi, \pi)$ to M. Without SOC, the two bands touch at an eight-fold degenerate contact point just below the Fermi level (figure 2(a)). SOC opens a gap at this touching point, leading to two new DNLs from A to M. It is worth mentioning that in the two-dimensional quantum spin Hall insulator model [52], a similar gap opening occurs in the bulk bands due to SOC, leading to robust topological edge states [52, 54, 74, 75]. In IrO_2, the gap opening does not occur at the Fermi level; however, it still contributes to the spin Berry

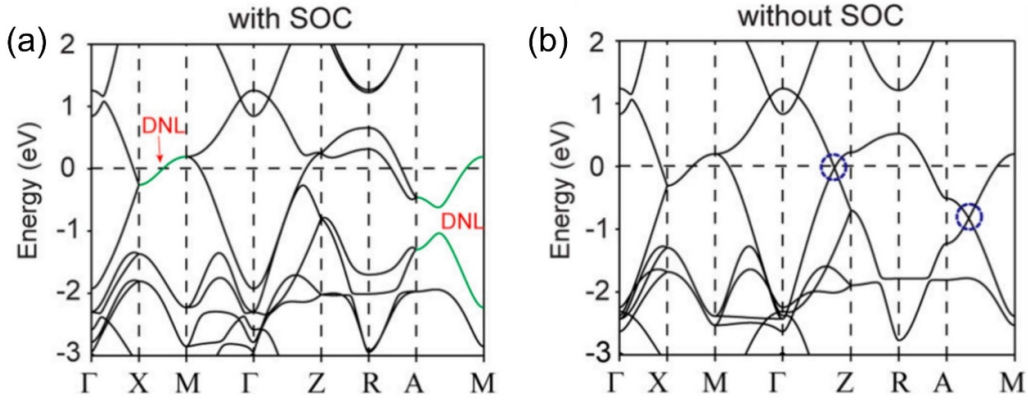

Figure 2. Calculated electronic band structures of IrO_2 (a) with and (b) without SOC. The bands highlighted with the green color in (a) represent the DNLs which are fourfold degenerate due to the nonsymmorphic symmetries. The dashed circles denote two Dirac points in the absence of SOC: the one along $\Gamma - Z$ path is sixfold degenerate, whereas the one along *A*–*M* is eightfold degenerate. Reprinted (figure) with permission from [71], Copyright (2019) by the American Physical Society.

curvature as the SOC-perturbed band (i.e. the upper DNL from *A*–*M* in figure 2(a)) passes through the Fermi level [48]. As will be discussed in section 2.4, the calculated band structure with SOC shows a good agreement with ARPES studies [50, 68, 71]. In addition, along *R*–*A*, the SOC-driven band splitting (about 0.4 eV) near the Femi level allows for an optical transition that is consistent with the measured optical conductivity spectra [44].

2.3. Nonsymmorphic symmetry and Kramers' degeneracy

Beyond SOC, crystal symmetry dictates the band dispersion along the high-symmetry axes. Essentially, the fourfold degenerate DNLs are formed by the intersection of two doubly degenerate bands. It is well known from the anti-unitary principle in quantum mechanics that a twofold degeneracy must arise in a lattice satisfying time-reversal symmetry $\mathcal{T}$ and inversion symmetry P because the anti-unitary operator $P\mathcal{T}$ leaves the momentum invariant and has $(P\mathcal{T})^2 = -1$. Such twofold degeneracy in a band structure is referred to as the Kramers' degeneracy. Furthermore, a generic four-band Hamiltonian producing two doublet bands can be expressed as $H(\mathbf{k}) = h_0(\mathbf{k}) + \sum_{i=1}^{5} h_i(\mathbf{k})\Gamma_i$ with the Gamma matrices possessing $\{\Gamma_i, \Gamma_j\} = 2\delta_{ij} I_4$ for $i,j = 1$ to 5. Pertaining to parameter counting, the spectrum $E_{\pm}(\mathbf{k}) = h_0(\mathbf{k}) \pm \sqrt{\sum_{i=1}^{5} h_i^2(\mathbf{k})}$ in 3D momentum space can be fourfold degenerate only if $h_1 = h_2 = h_3 = h_4 = h_5 = 0$, which is impossible without any fine tuning [46, 76]. Thus, the fourfold degeneracy results from the underlying symmetry.

The rotational and translational symmetries in the tetragonal lattice of IrO_2 belong to the space group $P4_2/mnm$ (No. 136). The nonsymmorphic symmetry operations, which represent the combined actions of point group symmetry and fractional translation, are included in this space group. The nonsymmorphic symmetries and the time reversal symmetry play a key role in accounting for the origin of DNLs [46, 47]. In a spin-1/2 electronic system, the Kramers doublet at momentum $\mathbf{k}$ is represented as two Bloch states $\{|\Psi_{\mathbf{k}}\rangle, P\mathcal{T}|\Psi_{\mathbf{k}}\rangle\}$. The composite operator $P\mathcal{T}$ is also anti-unitary. Along some highly symmetrical path in momentum space, the Bloch states $|\Psi_{\mathbf{k}}\rangle$ are eigenstates of certain nonsymmorphic symmetry operators with complex eigenvalues due to the fractional translation. Therefore, it is possible to form additional anti-unitary operators whose square is equal to minus identity; [49, 77] this can result in two inequivalent anti-unitary operators, which leaves momentum invariant and establishes fourfold degeneracy. Such notion is applicable in both spinful and spinless systems. Sun *et al* [48] introduced two types of DNLs: one in the absence of SOC and the other in the presence of SOC. SU(2) spin rotational symmetry is preserved in the former case where $\mathcal{T}^2 = 1$, whereas in the latter $\mathcal{T}^2 = -1$ scenario, SU(2) symmetry is absent. The former corresponds to a spinless system, whereas the latter is characterized as spinful.

We first focus on the DNLs in the band structure with SOC (figure 2(a)). Sun *et al* [48] showed the two inequivalent anti-unitary operators in the context of the DNL along the path from *X* to *M*. The algebraic relations among the nonsymmorphic symmetry operators, time-reversal, and inversion at Brillouin zone (BZ) edges are exploited. The general studies of the nonsymmorphic symmetries on topological aspects of band structures can be found in earlier references [46, 78–84]. The Bloch states $|\Psi_{\mathbf{k}}\rangle$ with $\mathbf{k} = (\pi, k_y, 0)$ are invariant under the mirror symmetry $\mathcal{M}_z$, the action of which in spatial space is (x, y, z) $\rightarrow$ (x, y, $-z$) and in spin space is (σ_x, σ_y, σ_z) $\rightarrow$ ($-\sigma_x$, $-\sigma_y$, σ_z), and under the nonsymmorphic $\tilde{\mathcal{M}}_x$ whose action is (x, y, z) $\rightarrow$ ($-x + \frac{1}{2}, y + \frac{1}{2}, z + \frac{1}{2}$) together with ($\sigma_x$, σ_y, σ_z) $\rightarrow$ (σ_x, $-\sigma_y$, $-\sigma_z$). It is worthwhile to note the representation in spin space: $\mathcal{M}_z = i\sigma_z$ as it commutes with $\mathcal{T} = (i\sigma_y)\mathcal{K}$ and satisfies the mirror symmetry for spins (e.g. see [85]), $(i\sigma_z)^{-1}\sigma_{x,y}(i\sigma_z) = -\sigma_{x,y}$ and σ_z is invariant. Similarly, in spin space $\tilde{\mathcal{M}}_x = i\sigma_x$. With these properties, Sun *et al* [48] showed the invariants, spin and space combined, of the Bloch state along *X*–*M* are: $\mathcal{M}_z^2 = -1$, $\mathcal{M}_x^2 = -e^{-ik_y}$, $\{\mathcal{M}_z, \tilde{\mathcal{M}}_x\} = 0$, and, crucially, $(\tilde{\mathcal{M}}_x P\mathcal{T})^2 = -1$. Consequently, the quartet $\{|\Psi_{\mathbf{k}}\rangle, P\mathcal{T}|\Psi_{\mathbf{k}}\rangle, \tilde{\mathcal{M}}_x|\Psi_{\mathbf{k}}\rangle, \tilde{\mathcal{M}}_x P\mathcal{T}|\Psi_{\mathbf{k}}\rangle\}$ is degenerate and orthogonal. Apart from the spin polarization, they can be further labeled by their $\mathcal{M}_z$ eigenvalues, $i, -i, -i, i$, respectively.

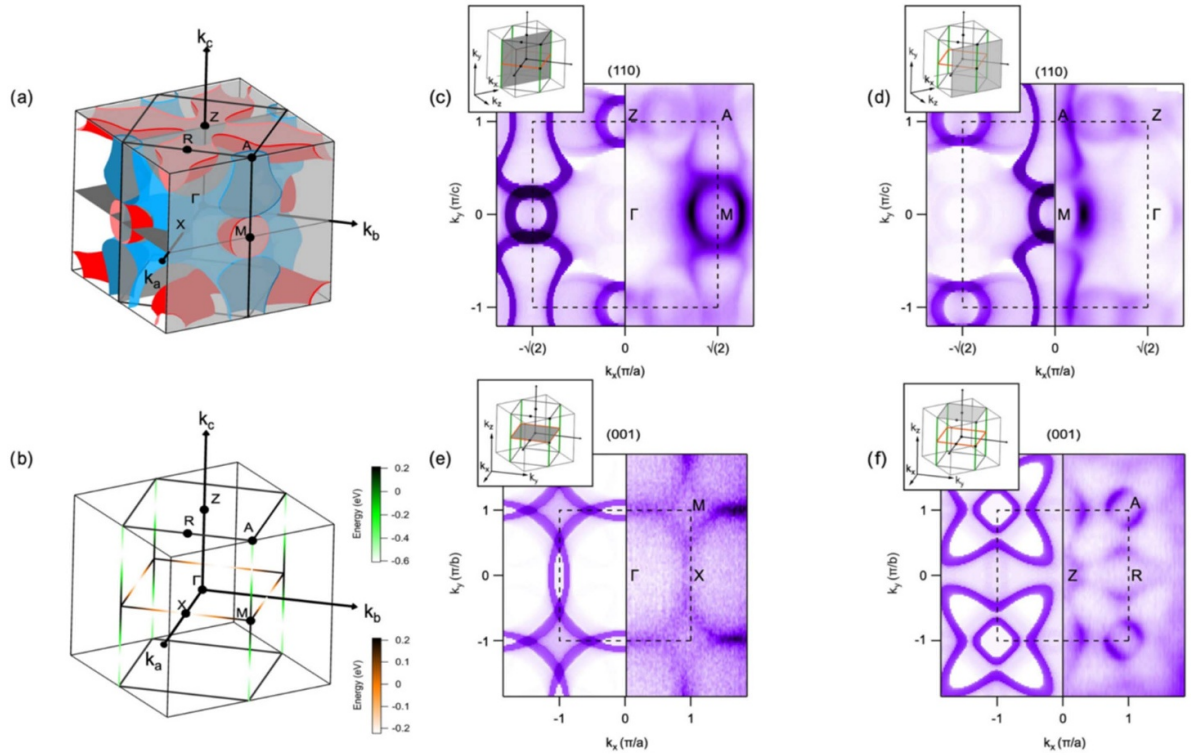

Figure 3. Fermi surfaces projected at (110) and (001) directions obtained by ARPES as demonstration of Dirac nodal lines in IrO_2. (a) Two hole-like Fermi surfaces (red) and one electron-like Fermi surface (blue). (b) Color-coded representation of Dirac nodal line dispersion along *A*–*M* and *X*–*M*. (c) The Fermi surface projected onto (110) central plane (inset), obtained from DFT (left) and ARPES (right). (d) The Fermi surface projected on (110) boundary plane. (e) and (f) Projections onto the (001) central and boundary planes, respectively. Reprinted (figure) with permission from [50], Copyright (2019) by the American Physical Society.

A similar argument can be applied to explain the fourfold degeneracy along *A*–*M*.

Next, we consider the band structure without SOC (figure 2(b)) and examine the origins of the DNLs; this helps understand the spin Hall effect that will be discussed in the subsequent subsection [51, 53]. Without SOC, the Hamiltonian commutes with all spin operators, SU(2) symmetry is restored, and each band is automatically two-fold degenerate. Li *et al* [49] provided examples of deriving Kramersdoublets when $\mathcal{T}^2 = 1$ in other nonsymmorphic materials, such as X_3SiTe_6 (X = Ta, Nb). One can show that along the path of $Z = (0, 0, \pi)$ to $R = (\pi, 0, \pi)$, for instance, the Bloch states are invariant under the combined $\tilde{\mathcal{M}}_x\mathcal{T}$, and the new Kramers doublet $\{|\Psi_{\mathbf{k}}\rangle, \tilde{\mathcal{M}}_x\mathcal{T}|\Psi_{\mathbf{k}}\rangle\}$ is an orthogonal set as $(\tilde{\mathcal{M}}_x\mathcal{T})^2 = e^{-ik_y - ik_z} = -1$. Moreover, the fact that the $k_x = \pi$ plane is a fourfold nodal plane [48] can be explained by the anti-unitary $P\tilde{\mathcal{M}}_x\mathcal{T}$. This is consistent with the SOC-free band structure (figure 2(b)), though we note that the degeneracy is indeed split when SOC is present.

It is interesting to note that the fourfold degenerate DNLs also appear in other iridates and nonsymmorphic systems. For example, the effective $J_{\text{eff}} = 1/2$ tight-binding band structure of orthorhombic $SrIrO_3$ displays fourfold degenerate bands along the paths *X*–*S* and *Z*–*T* [86]. Crystals in space group 135 have similar symmetry with IrO_2, and the generic and symmetry-preserved tight-binding model [47] also shows the fourfold degenerate bands along *X*–*M* and *M*–*A*. Along the paths, it can be seen that the original eight-band model reduces to a Hamiltonian consisting of anticommuting matrices only, which leads to two symmetric energy dispersions.

2.4. ARPES measurements of DNL semimetal states

The roles of symmetry on the formations of band touchings (points, lines, and planes) in the band structures of various topological materials have been reviewed extensively in [87]. For DNL semimetals, the *PT*-symmetry combining with nonsymmorphic symmetry constitutes a four-fold degeneracy among the Bloch states along some highly symmetric directions (see also section 2.3), with one-dimensional (1D) band touchings between two doubly degenerate bands even in the presence of SOC. The theoretically predicted band touchings in topological materials can be verified by ARPES measurements. Examples include the direct observations of time-reversal symmetry protected single Dirac cones on the surface of topological insulators (e.g. Bi_2Se_3 [88] and Bi_2Te_3 [89]), mirror-symmetry-protected pairs of Dirac cones on high-symmetry surfaces of topological crystalline insulators [90], as well as rotational-symmetry-protected Dirac points in bulk Na_3Bi [91, 92] along with Fermi arcs on its surfaces. In IrO_2, DFT calculations reveal the DNLs along *A*–*M* and *X*–*M*, and the calculated Fermi surface consists of two hole-like sheets and one electron-like sheet as shown in figure 3(a) [50]. The color-coded band energies along *A*–*M* and *X*–*M*

(figure 3(b)) indicate where the electron-like and hole-like sheets touch at the Fermi energy ($E = 0$). The Fermi surfaces obtained from the ARPES measurements along various directions match the theoretical predictions and hence verify the presence of DNL in IrO_2 [50]. Specifically, the Fermi surfaces projected on the (110) central plane in BZ (figure 3(c)) display the hole-like Fermi surface which has point contacts with two electron-like ones along *A*–*M*. Similar arrangement is also seen in the projection onto the (110) boundary plane (figure 3(d)), but an isolated Fermi circle is present around *Z* due to the SOC (see the band structures in figure 2(a) versus (b)). As for the (001) projection, figure 3(e) shows the Fermi surface with two contact points along *X*–*M* on the central plane in the BZ. Besides, the SOC-driven band split along *A*–*R* can explain the two disconnected Fermi surfaces projected on the (001) boundary plane in figure 3(f).

2.5. Relevance of DNLs to the spin Hall effect

Now we address the point of how the presence of DNLs (with and without SOC) is connected to the experimentally discovered spin Hall conductivity in the 3D IrO_2 [48]. The opening of the gap due to the SOC causes nontrivial topology associated with the Bloch wave functions and can lead to robust edge states capable of transporting spin and charge. One can understand this from the two-dimensional example proposed by Haldane in his seminal work of quantum Hall effect without magnetic field [74] where a two-band massive Dirac model $H(k_x, k_y) = k_x\tau_x \pm k_y\tau_y + m_\pm\tau_z$ describes the low-energy continuum in a honeycomb lattice. The Pauli matrices $\tau_{x,y,z}$ act in the sublattice space, while the $\pm$ sign refers to the two inequivalent *K* points in momentum space. A nontrivial topological phase arises when the mass terms $m_\pm$, due to the imaginary next-nearest neighbor hopping, have opposite signs at $\pm K$. The pseudo-spin associated with τ's forms a meron texture around $\pm K$ and as a whole is equivalent to a skyrmion texture [77, 93]. The imaginary hopping breaks the time-reversal symmetry, leading to one-way propagating edge states like the quantum Hall effect. The quantum spin Hall model proposed in [52] can be regarded as a direct sum of two Haldane models with each block representing one spin polarization. To restore the time-reversal symmetry, the mass terms in the two blocks must have $m_{\pm,\uparrow} = -m_{\pm,\downarrow}$ (see the corresponding expression equation (3) for SOC in [52]). Counter-propagating edge states carrying opposite spin polarization then appear at the edge. Generalizing the ideas to higher dimensions, 3D topological materials can be constructed by stacking such two-dimensional Dirac systems, but the mass term must then be a smooth function of momentum k_z. Burkov and Balents [94] proposed alternatively stacking the topological insulator and trivial insulator layers with a periodic width *d*. When the surface of the topological insulator layers is doped with magnetic impurities, the tight-binding Hamiltonian has the low-energy spectrum of the Weyl Hamiltonian $H = k_x\tau_x + k_y\tau_y + m(k_z)\tau_z$ around the two Weyl points $(0, 0, \pi/d \pm k_0)$ with k_0 determined by the strength of magnetic coupling. Importantly, the Weyl points signify the mass term changing sign $(m(k_z) < 0$ for $k_0 - |k_z - \pi/d| > 0)$. The segment of momentum along the k_z axis corresponding to the negative Dirac mass term contributes to transverse Hall conductivity.

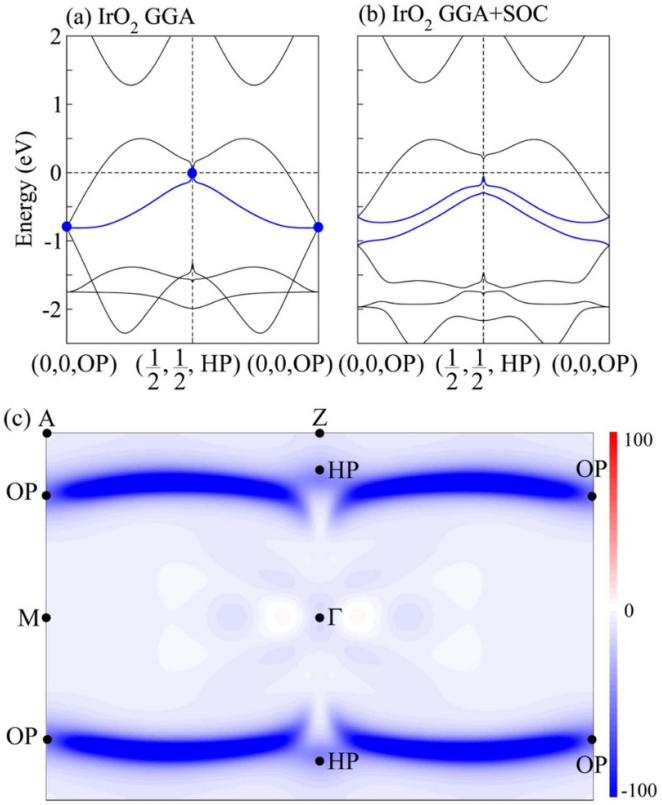

Figure 4. One-dimensional band dispersion along the path joining the Dirac points OP and HP on the (110) mirror plane. (a) and (b) are the results with and without SOC, respectively. Note that in (b)the band degeneracy is fully lifted at HP while the two-band touching remains at OP (OP located along *A*–*M*). (c) Displays the distribution of the spin Berry curvature along the (110) plane passing through the Dirac points as well as these highly symmetric momenta Γ, *A*, *M*, and *Z*. The gap opening [blue curve in (a) is split into their counter parts in (b)] due to the SOC results in significant spin Berry curvature. Reprinted (figure) with permission from [48], Copyright (2017) by the American Physical Society.

The above examples demonstrate that the SOC-induced gap opening in the region close to DNLs may contribute to a significant spin Berry curvature. Across the DNLs, which can be regarded as a continuum of Dirac points, the Dirac mass terms must change sign. Indeed, Sun *et al* [48] showed a spin Berry curvature contributed by the SOC-split bands inside the (110) mirror plane. Comparing the band structures with and without SOC, it can be seen that the band touching at points OP and HP (cf figures 4(a) and (b)) are open due to SOC, and the significant spin Berry curvature appears in the narrow stripe perpendicular to the DNL along the path *A*–*M*. The resultant spin Hall conductivity not only depends on the strength of SOC but also on the relative location of the split bands, the Fermi level, and the charge conductivity. Sun *et al* [48] computed the values of spin Hall conductivity for IrO_2, OsO_2, and RuO_2. While OsO_2 does not have the strongest SOC among the three materials, it has the largest spin Hall conductivity as a band gap is opened around the Fermi level [48].

3. Synthesis

The experimental demonstration of exotic electronic states and other fundamental properties in general requires the controlled synthesis of high-quality materials. Over the past few decades, IrO_2 has been successfully synthesized in various types of forms, including bulk crystals, thin films, nanorods, nanowires, nanotubes, and more. The growth methods are versatile, ranging from chemical vapor transport (CVT), physical vapor deposition (PVD), chemical vapor deposition, to chemical solution methods. In many of these synthetic experiments, the growth parameters can be controllably tuned to achieve the targeted structure, crystalline quality, composition, and size. In this section, we will first introduce the synthesis of bulk single crystals and then focus on the recent progress in the PVD growth of thin films and bottom-up synthesis of quasi-1D nanostructures that serve as a foundation for the study of their topological electronic and transport properties.

3.1. Bulk crystal growth by CVT

The CVT synthesis method embodies a series of chemical reactions in which an initial solid or liquid reacts with a transport gas and decomposes into vapor phase reaction products. The latter are transported through a gradient of temperature or pressure and are reformed into desired purified crystalline samples. CVT can be conducted in open or closed systems, in which the glass or ceramic tubes are either open or sealed on both sides [95]. During an open growth setup, the transport carrier gas continuously flows through the system and moves the precursors from a location at one temperature to a secondary location in a higher or lower temperature region. Conversely, in a closed system, a sealed tube or ampoule of glass contains generally a small amount of precursor which remains in the system and continuously participates in the reaction. Additionally, it contains as much transport agent as needed to achieve the required pressure [95].

CVT growth in an open system has been widely used to achieve high quality, bulk single crystals of IrO_2 [42, 96–99]. In a typical growth, pure Ir or polycrystalline IrO_2 (or a combination of the two) acts as the precursor, and a pure O_2 gas as the transporting agent [42, 96, 97, 99–101]. Various chemical reactions are possible [102]: (1) Ir metal can react with the O_2 around ∼1000 °C and develop solid IrO_2 layers; (2) Ir or (3) IrO_2 can combine with O_2 to form another oxide species, gaseous IrO_3, at an elevated temperature (T_2) of 1150 °C. When the iridium oxide vapors are then carried to a lower-temperature region (T_1) across the temperature gradient, a reverse reaction occurs in vapors, where the IrO_3 dissociates back into solid IrO_2 crystals of various sizes in a temperature range between ∼1000–1100 °C [96]. Ryden and Lawson observed several different crystal-growth habits based on the temperature distribution and oxygen flow rates, where they achieved [001] and [011] IrO_2 needles and (011) and (100) IrO_2 plates [100]. Reames reported that the variations in temperature parameters (i.e. oxidation temperature, growth temperature, temperature gradient) and gas flow rates led to a broad growth window for IrO_2 single crystals, within which no significant influence on the crystal quality was observed [96]. Both Reames [96] and Butler and Gillson [42] found that the O_2 pressure, on the other hand, did have a substantial impact on the growth results, presumably because it directly influences the formation and dissociation of IrO_3 [96]. For instance, crystals exhibited poor quality when O_2 pressures were 1 atm or lower due to excessive intergrowth that hindered the growth of crystals even ∼1 × 1 × 3 mm in size. Conversely, both the size and the shape of the crystals were clearly improved as the pressure was increased [42, 96]. In growths performed by Reames at higher oxygen pressures of 20 psi and 45 psi, single crystals of 1 × 1 × 5 mm and 3 × 3 × 2 mm, respectively, were obtained [96].

Beyond purely IrO_2 single crystals, mixed/doped single crystals have also been realized through CVT [96, 103]. Using $(Sn,Ir)O_2$ as an example [96], SnO_2 and IrO_2 are crystallographically similar as they possess rutile structures with similar lattice parameters but vary in their electrical and optical properties. While IrO_2 is an opaque conductor, SnO_2 is a transparent wide band-gap semiconductor. The mixed SnO_2:IrO_2 crystals appear transparent as well and are good candidates for optical studies. The growth method was similar to the previously described method used for IrO_2 single crystals, but a mixture of 85% Sn and 15% Ir metal powder was used as the precursor, the transport gas was air at 1/3 atmosphere, and the high temperature T_2 zone was 1475 °C [96].

3.2. Thin film growth by PVD

3.2.1. Pulsed laser deposition (PLD) of IrO_2 thin films. PLD is one of the most versatile PVD techniques for the growth of TMO thin films and heterostructures. In a PLD process, a pulsed laser strikes the surface of a solid target and ejects a plume of material (with nearly the same stoichiometry as the target) towards a substrate positioned in front, where a film is deposited. Earlier PLD growths of IrO_2 thin films were conducted on silicon or silicon oxide substrates using Ir metal as a target [104–111]. Although iridium has a low vapor pressure, laser ablation can readily vaporize the surface of the Ir target and create an iridium plume which reacts with the background O_2 gas to form IrO_2 thin films. The as-grown films are all polycrystalline due to the large lattice mismatch between the film and the Si substrate as well as the formation of amorphous silicon oxide layer at the substrate surface prior to deposition. Textured IrO_2 films were achieved by replacing Si with $SrTiO_3$ substrates, which have a relatively smaller (yet still large) lattice mismatch with the films [112]. Instead of Ir metal, IrO_2 was chosen as the target in this growth, although the precise influence of the target material on the film quality has not been explicitly studied [112]. Epitaxial thin films were realized when single-crystalline TiO_2 substrates were used (figures 5(a)–(c)) [44, 113]. The two binary metal oxides IrO_2 and TiO_2 have the same rutile structure with moderate lattice mismatches of $\sim -2.1\%$ in the a and b-axes and $\sim 6.6\%$ along the c-axis. Consequently, the epitaxial IrO_2 films present different degrees of compressive or tensile strains depending on the substrate orientation and

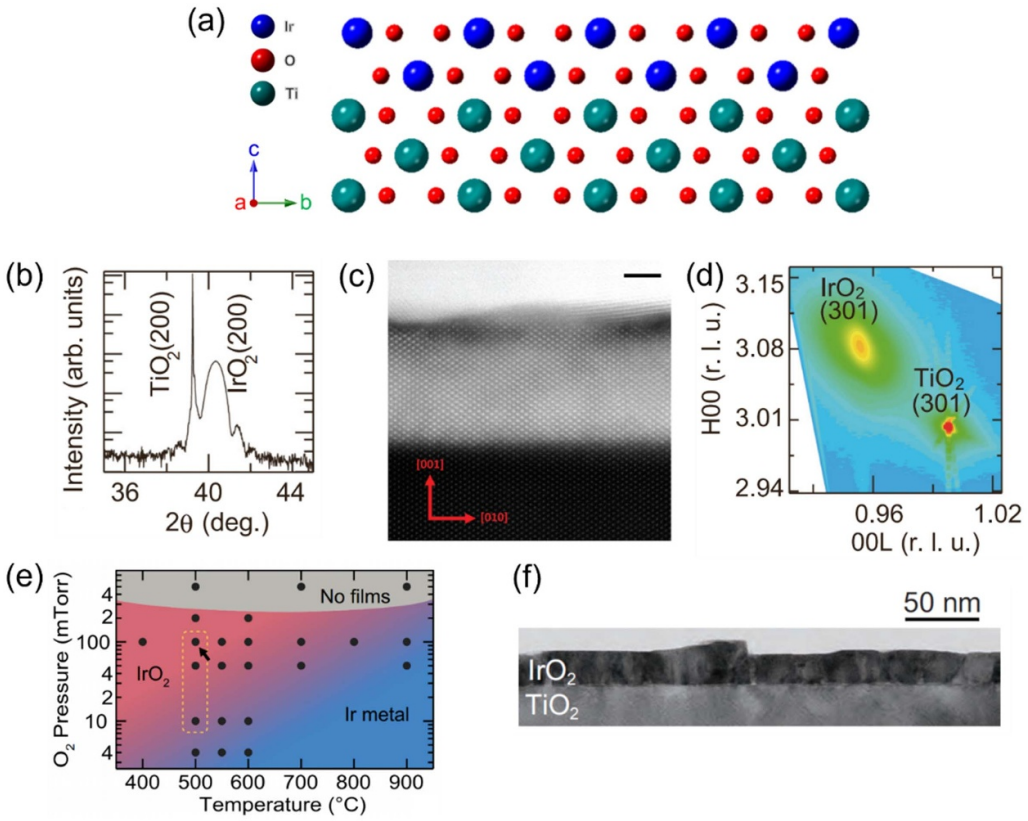

Figure 5. (a) A schematic illustrating the crystal structure of IrO_2 (100) thin film on TiO_2 (100) substrate. (b) X-ray diffraction (XRD) $\theta - 2\theta$ scan of a PLD-grown IrO_2 film on a single crystalline TiO_2 (100) substrate. (c) Cross-sectional scanning transmission electron microscopy (STEM) image showing a sharp interface of the epitaxial IrO_2 film and TiO_2 substrate. The scale bar is 2 nm. (d) X-ray reciprocal space mapping around the (301) Bragg reflections. (e) A PLD growth phase diagram describing the influence of O_2 pressure and deposition temperature on the IrO_2 films: no films are formed at high O_2 pressure regime, pure IrO_2 at intermediate O_2 pressures and relatively low temperatures, and films with Ir metal cluster at intermediate O_2 pressures and high temperatures. Each dot denotes a growth at the corresponding condition. The yellow dashed line and the arrow mark the optimal and the best growth conditions, respectively. (f) A cross-sectional TEM image showing the height difference between grains in a PLD grown IrO_2 film. (b), (d) Reprinted (figure) with permission from [44], Copyright (2016) by the American Physical Society. (c) Reproduced from [113] with permission from the Royal Society of Chemistry. (e), (f) Reprinted from [114], Copyright (2017), with permission from Elsevier.

film thickness, as evidenced by x-ray reciprocal space mapping characterizations (figure 5(d)) [44, 113].

In the PLD growths, O_2 pressure and substrate temperature are known to play an essential role in the stoichiometry and phase purity of the films. In general, Ir metal clusters can easily form in a low O_2 pressure and at a high temperature, whereas high O_2 pressure favors the volatile IrO_3 phase [115], resulting in significant Ir loss during the growth. It is also worth noting that the Ir metallization and high volatility of IrO_3 have been common challenges in the PLD growth of many other iridates thin films [116–122], although the extent of the challenges appear dependent on the particular crystal structure and composition of the iridates. As a result, one must cooperatively tailor the O_2 pressure and substrate temperature to achieve stoichiometric films free of Ir metal impurities. Hou *et al* [114] performed an array of systematic growth experiments and established a phase stability diagram for the IrO_2 films (figure 5(e)), where the optimal O_2 pressure and substrate temperature were found to be 10–100 mTorr and 500 °C, respectively. The epitaxial films grown at the optimal condition, however, were fully strain-relaxed. This was attributed to the nucleation of misfit dislocations at the initial growth stage which eventually led to the formation of columnar grain structures. Each individual grain has atomically flat surfaces, but the height difference between grains was as large as 5 nm for a 15 nm thick film (figure 5(f)). Islands were clearly observed after the deposition of the first couple of atomic layers, suggesting the growth mode is not layer-by-layer. While the O_2 pressure during the deposition strongly affects the phases (Ir vs. IrO_2), conditions used in a post-annealing process seem to have negligible influences [123], indicating the stability of the as-grown films.

Beyond single-phase thin films, IrO_2-based heterostructures have recently been grown by PLD, as well. Heterostructures containing spin-orbit coupled IrO_2 and ferromagnetic γ-Fe_2O_3 were deposited on Al_2O_3 (0001) substrates for inverse spin Hall effect studies [124]. The IrO_2 layer was deposited on the γ-Fe_2O_3 film at a relatively low temperature (325 °C) and an optimal O_2 pressure of 50 mTorr. Due to the different crystal structures between rutile IrO_2 and maghemite Fe_2O_3, the IrO_2 films were not epitaxially grown; nevertheless, a strong texture along the (100) orientation was observed,

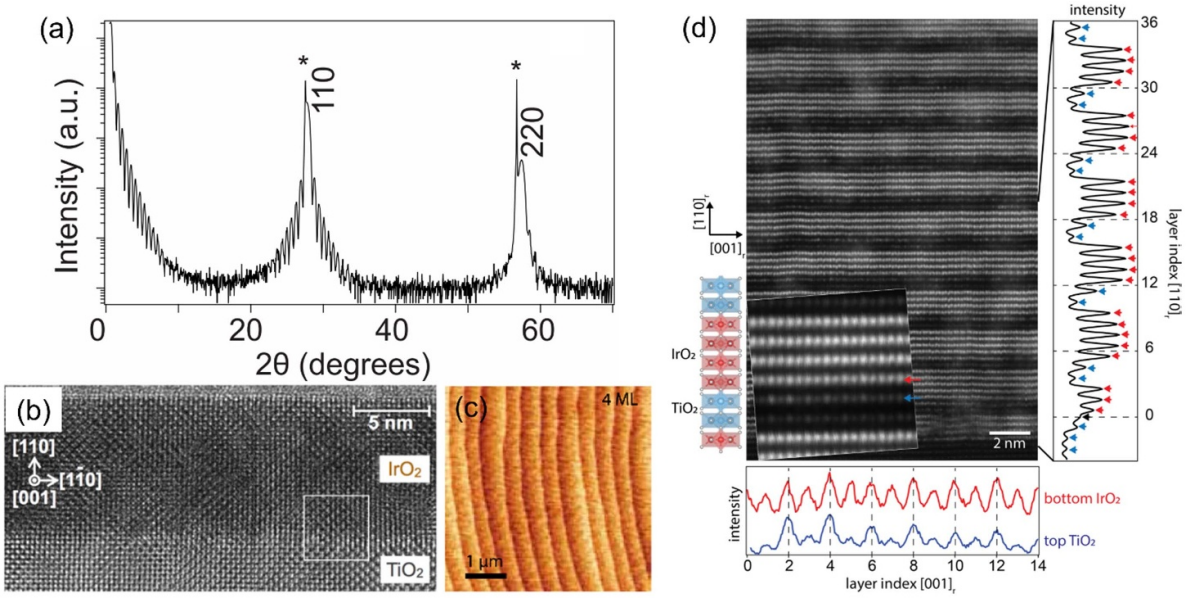

Figure 6. (a) XRD θ–2θ scan of an MBE-grown epitaxial IrO_2 thin film on a single crystalline TiO_2 (110) substrate. (b) Cross-sectional HRTEM image of an IrO_2 thin film. (c) Atomic force microscopy image of a four monolayer-thick film showing the step-and-terrace morphology. (d) Cross-sectional annular dark field-STEM image of an $(IrO_2)_4/TiO_2$ superlattice, and line scans along the [001] direction (bottom panel) and [110] direction (right panel). (a) Reprinted (figure) with permission from [45], Copyright (2016) by the American Physical Society. (b) Reprinted (figure) with permission from [126], Copyright (2015) by the American Physical Society. (c) Reprinted (figure) with permission from [125], Copyright (2018) by the American Physical Society. (d) Reprinted (figure) with permission from [127], Copyright (2018) by the American Physical Society.

which shows a significant influence on the spin Hall transport in the heterostructures.

3.2.2. Molecular beam epitaxy (MBE) growth. High-quality epitaxial thin films of IrO_2 with large-scale atomically smooth surfaces were realized by the Shen group [45, 50, 125] and the Kawasaki group [126] using MBE. Unlike in PLD, the Ir flux in MBE was supplied by electron beam evaporation of the elemental Ir source. To maintain a low-pressure MBE condition, distilled pure ozone was used as a highly reactive oxidant at a background pressure of 10^{-6} Torr. This contrasts with PLD which typically operates at a much higher O_2 pressure (e.g. 10–100 mTorr for IrO_2), as the laser ablated species are sufficiently energized to reach the substrate even after colliding with a high density of background gas. The substrates in the MBE growth of IrO_2 were again rutile TiO_2 with varied crystallographic orientations. The optimized substrate temperatures were about 300 °C, lower than the 500 °C in PLD which presumably has a faster deposition rate. Real time monitoring of the growth using reflection high-energy electron diffraction suggested that the IrO_2 films were grown in a layer-by-layer mode in a MBE process [125]. X-ray diffraction (XRD) and transmission electron microscopy (TEM) studies confirmed the single crystalline nature of the films (figures 6(a) and (b)). The surfaces of the films were atomically smooth, as evidenced by the sharp Kiessig fringes in the XRD $\theta - 2\theta$ pattern (figure 6(a)) and the step-and-terrace-like surface morphology (figure 6(c)) which resembles the surfaces of the single-crystalline TiO_2 substrates [45, 50, 125, 126]. The atomically smooth films with high-crystalline quality have offered an excellent platform for the *in situ* ARPES studies of electronic structures [45, 50, 125].

Furthermore, all-rutile IrO_2/TiO_2 superlattices were epitaxially grown by MBE on [110]-oriented TiO_2 substrates [127], in spite of the moderate lattice mismatch (6.6% in *c*-axis and −2.1% in a and b) between the two binary oxides. The superlattices have a periodicity of $n = 3, 4, 5$ atomic layers, and all the expected superlattice reflections were observed in the XRD. Atomically sharp interfaces were directly visualized by cross-sectional scanning TEM (STEM, figure 6(d)). The STEM intensity line scans indicate a possible interfacial reconstruction in the TiO_2 layer, which partially released the strain at the interface and promoted a growth of superlattices with high structural quality regardless of the lattice mismatch. The success in the superlattice growth is also associated with the low energy of the (110) surfaces of the two rutile oxides, as the growth of [001]-oriented superlattices with high (001) surface energy has turned out to be challenging [127].

In a modified MBE growth, Nair *et al* [128] replaced the pure elemental Ir source with Ir-organic precursor which has a significantly higher vapor pressure and thus requires a much lower source temperature (<200 °C). Interestingly, their growths produced phase pure Ir or IrO_2 films, which was exclusively dependent on the choice of substrates. To be specific, a (110)-oriented TiO_2 substrate favors the growth of IrO_2, whereas *c*-plane sapphire substrates promote the growth of pure Ir metal films. Since those depositions were performed at

identical oxidation conditions, the different phases of the as-grown films emphasize the important role of lattice-mismatch-induced-strain in dictating the oxide formation enthalpy.

3.2.3. Sputtering growth. Sputtering is another common PVD technique for the growth of IrO_2 thin films, particularly owing to its strong capability of sputtering materials with high melting points (e.g. 2446 °C for Ir in this case). The sputtering growth of IrO_2 has a longer history than the PLD and MBE growths. In the 1970s and 1980s, the main purpose for the sputtering of IrO_2 was to study its electrochemical properties for potential applications in chemical sensing, electrocatalysis, and electrochromic devices [129–133]. Most of these growths were conducted on Si substrates via reactive sputtering of Ir targets in a mixed O_2/Ar atmosphere [134]. The as-grown IrO_2 films were polycrystalline or partially amorphous, depending on the deposition temperatures. Like in the PLD growth, the O_2 partial pressure and deposition temperatures play a crucial role in determining the phases (i.e. Ir versus iridium oxides) of the films, whereas substrates strongly influence their crystalline quality [135–138]. The recent interest in the sputtering growth has been mainly motivated by the exotic spintronic properties of IrO_2. Epitaxial thin films were realized on single-crystalline TiO_2 substrates either in a pure O_2 atmosphere [113] or in an O_2/Ar gas mixture [139]. Heterostructures composed of spin-orbit-coupled IrO_2 and ferromagnetic permalloys, such as $Ni_{81}Fe_{19}$ and $Co_{40}Fe_{40}B_{20}$, were deposited *in situ* in DC or RF sputtering systems for spin transport studies [140–144]. The depositions were conducted either at room temperature followed by a post-annealing process [141] or directly at elevated temperatures [140, 142]. The substrates were Si/SiO_2 or TiO_2, which again yields polycrystalline [140, 141] or epitaxial IrO_2 layers [142], respectively. Since the layer uniformity impacts the spin transport across the interface, the substrates were typically rotated during the deposition to ensure that each layer has a uniform thickness. Using co-sputtering deposition, various doped IrO_2 films have also been grown recently, including $Ir_{1-x}Sn_xO_2$ [145], $Ir_{1-x}Co_xO_2$ [146], and $Ir_{1-x}Cr_xO_2$ [147], which are either amorphous or polycrystalline depending on the specific growth conditions.

3.3. Growth of (quasi-)1D nanostructures

3.3.1. Metal organic chemical vapor deposition (MOCVD). (Quasi-)1D nanostructures of IrO_2, with various morphologies including nanorods [148–152], nanotubes [153], and nanowires [154], were first grown by MOCVD, where the precursor was (methylcyclopentadienyl) (1,5-cyclooctadiene) iridium (I). Pure O_2 was introduced as both the carrier gas and reactant [148, 154]. Chen *et al* [148] managed to convert the IrO_2 thin film growth into a nanorod growth on Si substrates by increasing the MOCVD chamber pressure from 1 Torr to 30 Torr in a pure O_2 environment at 350 °C. The as-grown nanorods were found to be greater in density and better aligned in the vertical direction when the Si substrate was coated with Ti metal [149]. By controlling the precursor temperature T_{pr} and the substrate temperature T_s, a series of 1D nanostructures were grown with diverse morphologies such as triangular and square nanorods, incomplete and square nanotubes, as well as scrolled nanotubes (figures 7(a)–(c)) [150]. In general, T_{pr} is a direct way to control the supersaturation $\Delta\mu$ which is a driving force for the growth, whereas T_s is critical to the surface kinetics and has significant influence on the surface morphology of the nanostructure. Therefore, different morphologies can be achieved by systematically tuning T_{pr} and T_s. From the perspective of surface kinetics, lower $\Delta\mu$ and higher T_s provide more diffusion time and energy for the adhered surface atoms to arrange and diffuse, thus forming structures with a more thermodynamically stable morphology. Solid nanorods with square cross-sections are more energetically favorable compared to other complex 1D structures, thus they were grown at relatively lower supersaturation (T_{pr}) and higher T_s [150]. However, at the lowest T_{pr} and highest T_s in the studied range, 1D nanostructures no longer exist; instead, a film composed of 3D grains is the most morphologically stable and hence is formed [150].

Although coating the growth substrates with metal nanoparticles increases the density of nanorods/nanowires [154], the 1D nanostructure growth is through a direct vapor–solid (VS) deposition rather than a metal-catalyzed vapor–liquid–solid (VLS) process as typically seen in semiconductor wire growths [156]. Indeed, IrO_2 nanowires have been grown on bare Si or SiO_2 substrates without the use of metal particles. The increase in nanowire density by coating metal particles on the substrates was attributed to the enhanced absorption of atoms onto the substrate and the facilitated nucleation for nanowire growth [154]. It is not fully understood as to why the VS process gives rise to 1D anisotropic growth of nanowires, but all of the reported IrO_2 nanorods/nanowires were grown along the [001] direction (or the *c*-axis) of the rutile phase, and the major facets were (110) planes (figure 7(d)). This is consistent with the (110) plane having the lowest surface energy, whereas the (001) plane has the highest surface energy among the low index surfaces [157]. As schematically illustrated in figure 7(e), the adatoms deposited on the (110) surfaces tend to diffuse to the (001) surface where they nucleate and grow. This process increases the area of the (110) facets while maintaining that of the (001) surface, which minimizes the total surface energy and leads to a quasi-1D growth along the [001] direction.

The crystal structure and orientation of the substrate has a strong influence on the alignment of the 1D nanostructures that are epitaxially grown on it. For example, nanotubes were vertically aligned on $LiNbO_3$ (100) substrates [155], but tilted on the $LiTaO_3$ (012) substrates [153]. A fundamental reason is that the formation of the IrO_2 crystal plane on the substrate always tends to minimize its lattice misfit with the substrate and lower the strain energy at the interface. IrO_2 (001) has the best lattice match with the $LiNbO_3$ (100) plane, whereas IrO_2 (101) matches well with the $LiTaO_3$ (012). Since the 1D nanostructures grow along the [001] direction, they were perpendicular to the surface of the $LiNbO_3$ (100) substrate but made an angle of 55° with the $LiTaO_3$ (012) surface (figures 7(f) and (g)).

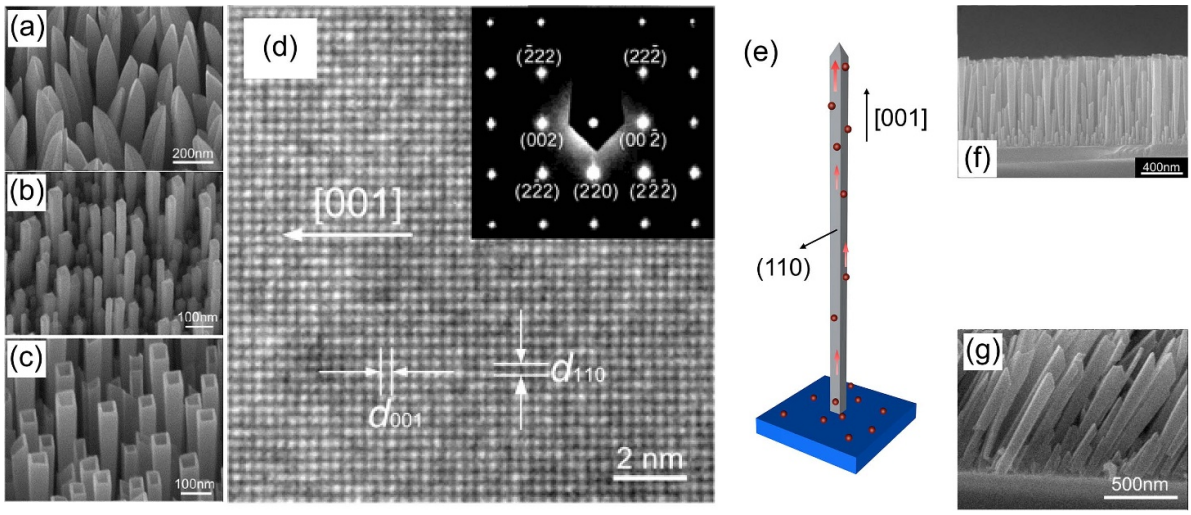

Figure 7. (a)–(c) One-dimensional structures of IrO_2: triangular nanorods, square nanorods, nanotubes. (d) HRTEM image of an IrO_2 nanotube grown along [001] direction. Inset: a selected-area electron diffraction pattern. (e) A schematic showing the adatoms tend to diffuse towards the (001) surface to minimize the total surface energy. Scanning electron microscopy (SEM) images of (f) vertically aligned nanotubes grown hetero-epitaxially on $LiNbO_3$ (100) substrate and (g) tilted nanotubes (by an angle of 35°) grown hetero-epitaxially on the $LiTaO_3$ (012) substrate. (a)–(c) Reproduced from [150]. © IOP Publishing Ltd All rights reserved. (d), (g) Reprinted with permission from [153]. Copyright (2004) American Chemical Society. (f) Reprinted from [155], Copyright (2004), with permission from Elsevier.

3.3.2. Vapor phase growth. The 1D nanostructures grown by MOCVD are typically shorter than 2 μm, making it very challenging to fabricate four-terminal devices and limiting their feasibility for advanced transport studies. Single-crystalline IrO_2 nanostructures with lengths up to tens of micrometers have been grown via a vapor phase transport method in a single-zone tube furnace where IrO_2 powder was used as a precursor. The growth took place either on SiO_2/Si substrates [158] or on Au [158] and Pt [159] microwires which were positioned downstream from the precursor boat. The nanowires were grown out of plane in random orientations with a non-uniform diameter, resembling a needle-like shape (figure 8(a)). No catalyst particles were observed at the tip of the nanowires, suggesting the growth is through a VS process instead of VLS, like in the case of the MOCVD growth. In the growth process, solid IrO_2 powder placed within the high temperature zone was first oxidized into volatile gaseous IrO_3 species due to the flow of O_2 into the reactor. As such, the vapor phase is essentially created via a chemical process instead of a physical approach like in PLD or sputtering. The IrO_3 vapor was transported by the carrier gas (e.g., a mixture of O_2 and inert gas) onto the substrates located in a low temperature zone where it disassociated into IrO_2. For this reason, the flow of O_2 is essential to the growth. Indeed, no nanowires were grown without O_2, as the powder remained as IrO_2 or was reduced to metal Ir, both of which have much lower vapor pressure than IrO_3.

Single-crystalline IrO_2 nanowires with more uniform diameters and as thin as tens of nanometers were grown through a similar vapor phase transport process in a three-zone tube furnace [160]. The nanowire growth was enhanced through the independent control of temperature in different zones as well as the coating of Si substrates with IrO_2 powder prior to the growth. Furthermore, only inert Ar gas was flowed during the ramping up segment to prevent unwanted growth from occurring during this 'unstable' stage. The 'reactive' O_2 gas was introduced only after the growth temperature was stabilized. As shown in figure 8(b), the as-grown nanowires have a uniform diameter along the majority of the wire length with the exception of tapering at the tip. The absence of catalyst particles at the tip again confirms the growth is through VS, instead of VLS. The IrO_2 nanowires achieved in this work have smooth surfaces and well-defined cross-sectional shape (figures 8(c)–(e)), enabling the observation of a pure geometric effect in the electron diffraction measurement for the first time [160]. Beyond improving the morphology, the introduction of IrO_2 powder onto the substrate before the growth also tends to increase the nanowire density, similar to the growth of VO_2 nanowires [162].

Chemical doping was realized in the nanowire growth, as well [161, 163, 164]. In particular, single-crystalline $Ir_{1-x}V_xO_2$ nanowires were achieved on Si substrates using IrO_2 and VO_2 powder as precursors and a mixture of O_2 and Ar as reactive and carrier gas, respectively [161]. It is known from the undoped nanowire growth [154, 158, 162, 165–167] that IrO_2 prefers to grow in an O_2 atmosphere, whereas VO_2 prefers Ar. Thus, a mixture of O_2 and Ar is essential for the growth of doped nanowires. In the presence of O_2, highly volatile IrO_3 and V_2O_5 phases are expected to form and further react with each other as they dissociate on the substrate to realize V-doped IrO_2 nanowires through a direct VS process. The composition of the nanowires can be tuned not only by the relative temperatures of the two precursors but also by the ratio of O_2/Ar which directly influences the formation of volatile IrO_3 and V_2O_5. The nanowires grown using this approach were smooth and straight and exhibited diameters down to ~40 nm and lengths up to tens of micrometers long. The density of achieved nanowires was increased by scratching the

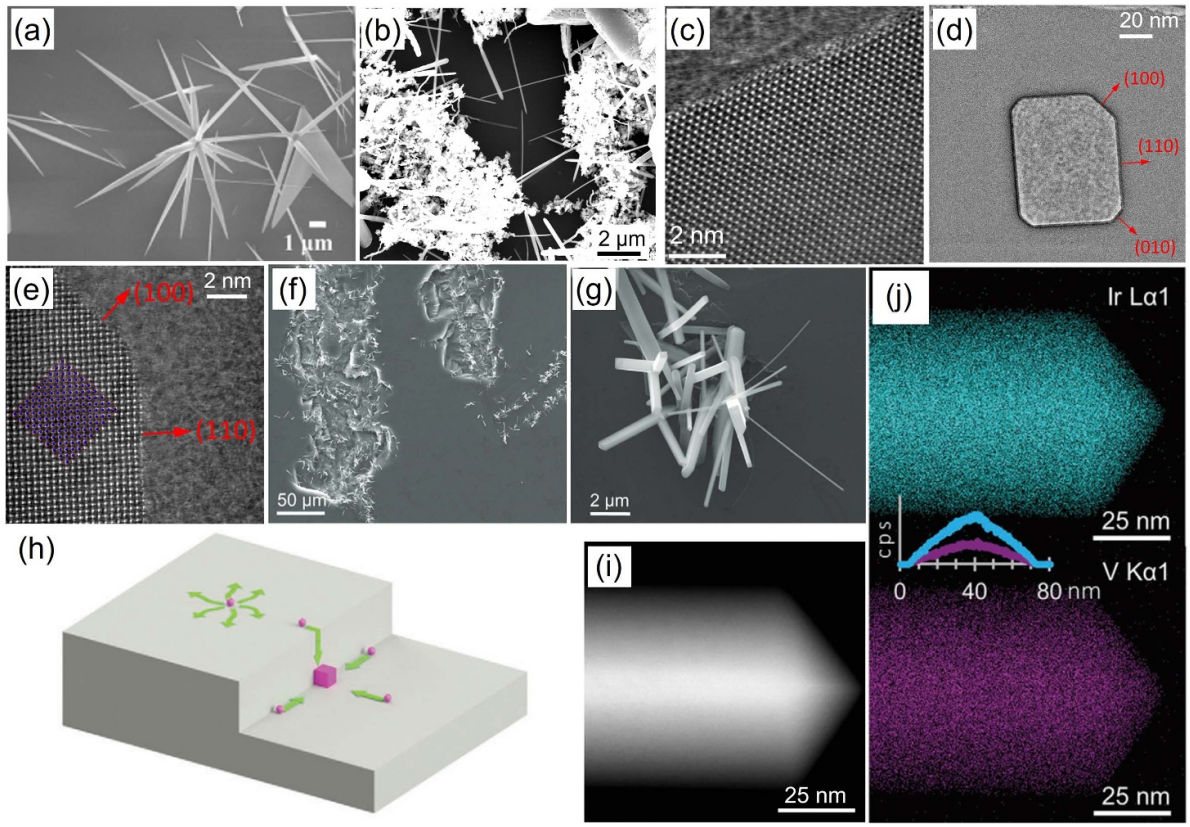

Figure 8. SEM images of (a) needle-like IrO_2 nanowires grown by vapor transport and (b) less-tapered nanowires grown by a modified vapor transport approach where IrO_2 powder was coated on the substrate to facilitate growth. (c) An optimum bright-field (OBF) STEM image demonstrating the high crystalline quality of an IrO_2 nanowire near its surface. (d) and (e) OBF images taken at different magnifications with the e-beam parallel to the nanowire axis to show its cross-section. (f)–(g) SEM images at different magnifications revealing the enhanced nanowire density in the scratched region of a Si substrate. (h) A schematic drawing illustrating the different diffusion preferences of adatoms in the flat region and near an edge. Atoms diffuse isotopically in the former case, whereas they tend to diffuse towards the edge in the latter case, which generally enhances nucleation. (i) High-angle annular dark-field STEM image and (j) energy-dispersive x-ray spectroscopy (XEDS) maps of a V-doped IrO_2 nanowire near its tip. The inset shows the XEDS line scans of Ir (cyan) and V (purple) across the nanowire diameter. (a) Reprinted with permission from [158]. Copyright (2012) American Chemical Society. (c)–(e) Reprinted from [160], Copyright (2023), with permission from Elsevier. (f)–(h) and (j) Reproduced from [161]. CC BY 4.0.

substrates before the growth to create fresh and rough surfaces, which facilitates the nanowire growth (figures 8(f) and (g)) [161]. As illustrated in figure 8(h), the adatoms tend to diffuse towards the edges [168–170] in the scratched areas where they interact with multiple surfaces. Such interactions reduce the energy required to form nucleation sites, resulting in an increased number of nucleation sites and hence an enhanced density of nanowire growth [171–173]. A similar enhancement of nanowire density was realized by using rough substrates in the growth of pure VO_2 wires [174]. The high quality and improved density of $Ir_{1-x}V_xO_2$ nanowires (figures 8(i) and (j)) enabled the fabrication of various nanodevices for electrical and thermal transport studies.

4. Transport studies

In IrO_2, the competition between the approximately equal energy scales of SOC and other interactions results in a diverse array of quantum states depending on strain, doping, dimensionality, temperature, magnetic field, and other parameters. The concomitant tunability of IrO_2 as host for quantum states of matter describes one of the attractions of the material, in combination with its relatively high metallic electrical conductivity. This section will describe the richness of the electrical, spin and thermal transport properties of IrO_2. The dimensionality (bulk form, thin or ultrathin films, or nanowire form) turns out to be a determining factor, not surprisingly, given the common theme of tunable properties. The transport properties illustrate the metallic transport characteristics and the tunability of the properties under external parameters, which include the appearance of a metal-insulator transition due to competition between enhanced U, the bandwidth, and the disorder potential in thin films, a tunability of the carrier type under magnetic fields due to the nonsymmorphic structure of IrO_2, and an orbital two-channel Kondo effect associated with oxygen vacancies. The strong SOC is of considerable interest in spintronics for spin-to-charge conversion or

vice-versa, as it results in a large spin Hall angle. The large atomic mass difference between Ir and O, strong interatomic bonding, and interactions between electrons and phonons give rise to unique thermal transport properties. The influence of chemical doping on transport will also be discussed.

4.1. Electrical transport

4.1.1. Bulk electrical transport properties. In DNL semimetals, such as IrO_2, the bands may cross along 1D closed loops in the BZ. The nodal loop carries a π Berry phase. Electronic transport properties are affected by the nodal line and by its Berry phase, and of particular note in the materials are Shubnikov–de Haas oscillations, a large positive magnetoresistance, and weak-localization/antilocalization effects [175]. Shubnikov–de Haas oscillations (quantum oscillations in resistivity) reflect the extremal cross-sectional areas of the Fermi surface perpendicular to the direction of the magnetic field, and their phases reflect the π Berry phase if the cross-section encloses the nodal line. Given the multiple extremal cross-sections of a toroidal Fermi surface, this set of rules results in a detailed diagnostic allowed by the oscillations but also in a complex set of oscillations requiring careful analysis and defying simple enumeration [175–179]. A large non-saturating and often anisotropic positive magnetoresistance is often observed [179–183], the origin of which continues to form the topic of discussion [179]. Several examples of the Shubnikov–de Haas oscillations and of the positive magnetoresistance are found in the literature [184–186]. Weak-localization and antilocalization are quantum corrections to the classical resistivity due to quantum interference on exact time-reversed closed carrier paths created by scattering events, and they result in characteristic magnetoresistances [116, 175, 187]. In DNL materials the toroidal Fermi surface affects the scattering mechanisms while the π Berry phase modifies the quantum interference [187], leading to observations of characteristic quantum corrections in several DNL materials systems [188–191].

Transport studies of IrO_2 bulk crystals were first conducted back in the 1970s, where a metallic behavior and oscillatory magnetoresistance were observed [100, 192, 193]. Magnetothermal oscillations (oscillations in sample temperature versus magnetic field) in early work on rutile single-crystal IrO_2 [193] grown by the CVT, showed signatures of a complicated Fermi surface. Earlier related magnetoresistance measurements showed both Shubnikov–de Haas oscillations, and a monotonic positive magnetoresistance [192], anticipating the pronounced positive magnetoresistance described for DNL semimetals. Analysis of the combined works [192, 193] was interpreted in terms of a Fermi surface with several pancake-shaped and dumbell-shaped electron sections and cross-shaped hole surfaces. With hindsight of ∼50 years and present knowledge of DNL materials, the interpretation in terms of a complicated Fermi surface was not off the mark. Figure 9 shows magnetoresistance data from [192] obtained at 1.2–4.2 K at a fixed magnetic field of 10 T. The current was applied along [001] and the orientation of the magnetic field was varied over two angles (θ and ϕ in the figure) to reveal Shubnikov–de Haas oscillations attributed to different Fermi surface cross-sections.

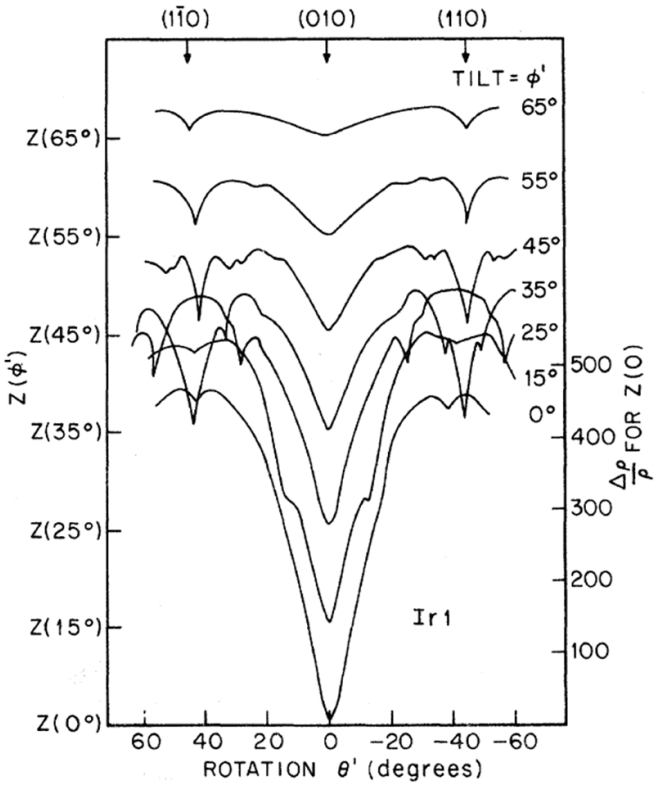

Figure 9. Magnetoresistance in rutile single-crystal IrO_2 at 1.2–4.2 K and at a fixed magnetic field of 10 T. The current was applied along [001]. Using sample rotation, the direction of the magnetic field was varied over two angles θ (crystallographic direction indicated on top axis) and ϕ to obtain Shubnikov–de Haas oscillations due to various Fermi surface cross-sections. The magnetoresistance is expressed as the relative change in resistivity ($\Delta\rho/\rho$) and its scale is arbitrary. The zero is offset for each ϕ (indicated by Z on the left axis). From the data, a model of a complicated Fermi surface was deduced. Reprinted (figure) with permission from [192], Copyright (1972) by the American Physical Society.

More recently, Lin *et al* [98] re-examined the electronic transport properties of single crystals of IrO_2 and RuO_2 over the temperature (T) range 0.3 K to 300 K. Both TMOs adopt the same rutile structure and exhibit similar metallic transport properties, meaning that the electrical resistivity drops monotonously with decreasing T. The IrO_2, in particular, showed pronounced metallic behavior with resistivity ratios between 300 K to 4 K of 224–826. A fit of resistivity vs T to scattering of electrons with acoustic phonons (Bloch–Grüneisen model) and with optical phonons (Einstein model) showed good agreement with the models, demonstrating the importance of phonon scattering in accordance with the standard theory for metals. A Debye temperature of $\theta_D \approx 290$ K was deduced for IrO_2. While substantially more studies have been performed on thin films and nanowires, undoped IrO_2 in bulk

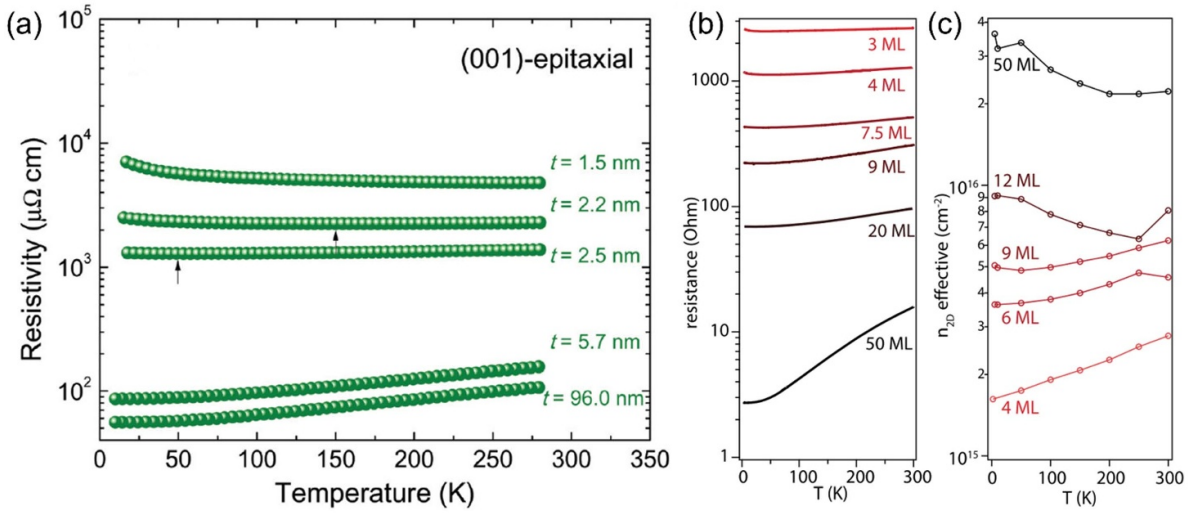

Figure 10. (a) Resistivity vs temperature in PLD-grown IrO_2 films on TiO_2 substrate with (001) orientation for different film thicknesses (measured in van der Pauw configuration). The upturn into insulating behavior, indicated by an arrow, denotes a metal-insulator transition appearing for the thinnest films of thickness 1.5 nm–2.5 nm. (b) Resistance vs temperature measured along the [001] direction of the [110]-oriented thin films grown by MBE with varied thicknesses down to 3 monolayers. (c) Effective 2D hole density of the MBE-grown films as a function of temperature. (a) Reproduced from [113] with permission from the Royal Society of Chemistry. (b), (c) Reprinted (figure) with permission from [125], Copyright (2018) by the American Physical Society.

form presents properties in accordance with good metallic behavior [100].

4.1.2. Thin film electrical transport properties. In thin film form, the additional parameter of lower dimensionality leads IrO_2 to display a richer spectrum of properties stemming from its crystal structure, DNL, and competition between energy scales as discussed earlier. At a fundamental level, the exotic behavior is however underpinned by good metallic properties, as shown in the transport properties of polycrystalline thin film IrO_2 obtained by RF sputtering on glass substrates measured in [194], between 15 K and 300 K (for similar RF sputtered polycrystalline films see [195]). The films exhibited the usual metallic behavior, dominated by acoustic and optical phonon scattering and impurity scattering, but also show that the additive Matthiessen's rule for phonon and impurity scattering is not followed for $T < 0.1\ \theta_D$. At low T, phonon and impurity scattering are not independent and an interference term due to scattering by vibrating impurities functions as an additional scattering mechanism (Reizer–Sergeev scattering). The interference term leads to a contribution to resistivity scaling as T^2 which was distinguished from electron-electron scattering. In IrO_2 the interference term can, at low T, dominate by a factor 10 over the Bloch–Grüneisen acoustic phonon scattering contribution. At higher T, acoustic phonon scattering dominates, succeeded at the highest T by optical phonon scattering.

Progressing from thin to ultra-thin films, IrO_2 shows thickness-dependent properties that illustrate a typical controllability of properties on external parameters, including dimensionality that affects the competition between bandwidth, correlations, and disorder, and may induce magnetic properties. Egido *et al* [113, 196] studied transport properties of IrO_2 thin films (grown by PLD and sputtering) as a function of film thickness down to few monolayers (MLs). A metal-insulator transition appears for the thinnest films in the 1.5 nm–2.5 nm range (3–5 unit cells), as illustrated in figure 10(a). Films above 3 nm are metallic over the measurement range (10 K–300 K), films of 2.5 nm-thick films show insulating behavior below 50 K, of 2.2 nm below 150 K, of 1.7 nm below 250 K, and films of 1.5 nm are insulating over the measurement range. The tunable properties of IrO_2 thin films include the bandwidth W, where W drops with decreasing thickness (similar to strain engineering). The ratio of U/W, where W and U denote the kinetic energy or electron hopping and the electron correlation energy, respectively, determines the importance of electron correlations. Higher U/W can lead to a Mott metal-insulator transition due to the formation of a Coulomb gap. Thinner films also accentuate the role of disorder, quantified by disorder potential D. A higher D/W in thinner films can yield the formation of an Anderson insulator. Whereas IrO_2 in bulk or thicker film form does not show magnetic ordering, magnetic ordering was reported in the magnetization measurement of the thinnest films, within the ultrathin film limit [113]. This antiferromagnetic order can lead to a Slater insulator. Mott, Anderson or Slater insulators are all candidates to explain the metal-insulator transition. For films of thickness 1.5 nm, the temperature dependent resistivity can be well fitted by the Efros–Shklovskii variable range hopping model due to Coulomb gap opening, indicative of a Mott insulator. Yet at 125 K a weak ferromagnetic-like transition is detected in the 1.5 nm (100) film, possibly developed from a canted antiferromagnetic order as observed in strontium iridate ($SrIrO_3$) thin films which also shows a metal-insulator transition as the film thickness is reduced to the ultrathin limit [197, 198]. As a result, a mixed Mott and Slater insulator may underlie the metal-insulator transition, as observed in figure 10(a).

The dimensionality also brings out properties associated with the DNL, as demonstrated by Kawasaki *et al* [125] describing ARPES and transport measurements (figures 10(b) and (c)) on MBE-grown ultrathin single crystalline IrO_2 (110) films on TiO_2 (110) substrates. The resistance vs T shows an overall metallic behavior, yet with a slight upturn in resistance with decreasing $T < 40$ K for films of 3 ML and 4 ML thickness (figure 10(b)). Such an upturn in ultrathin films was also observed in [113, 196]. While in these works a transition to a mixed Mott and Slater insulator was invoked, the upturn in [125] is ascribed to a confinement-induced quantization of the momentum vector normal to the growth plane for films below 10 ML. It is indeed evidenced that the carrier density, as expressed in 3D, drops sharply in films below 10 ML due to the formation of quantized subbands with accompanying energy gaps. In fact, the resistivity as expressed in 3D increases by about two orders of magnitude between 50 ML and 3 ML. Comparing results of [113, 196] with [125], it is plausible that contributions from either an interaction-induced Mott insulator or confinement-induced quantization can contribute to insulating behavior in ultrathin films, depending on disorder and growth conditions. Thurs, results have to be interpreted in the light of a specific experiment. Further, ARPES shows an enhancement of effective mass in the ultrathin films due to the quantum confinement in the specifically non-parabolic bands expected for a DNL semimetal. It is shown that electron-electron interactions do not have a large role in the effective mass enhancement, unlike in several other materials systems amenable to quantum confinement, such as in GaAs/AlGaAs heterostructures. The examples above demonstrate the tunability of IrO_2 thin films as hosts for quantum states of matter.

Tunability of the carrier type is demonstrated by Uchida *et al* [126] and is based on the rutile structure assumed by IrO_2. The rutile structure of IrO_2 is a typical nonsymmorphic crystal structure, which can lead to very anisotropic folded Fermi surfaces near the Brillouin zone boundaries. As a result, the dominant charge carrier type (electron or hole) can be expected to be anisotropic in crystal orientation and sensitive to the details of external stimuli. Indeed, Uchida *et al* [126] showed that the carrier type in IrO_2 indicated by the Hall effect switches depending on the measurement's magnetic field orientation, as depicted in figure 11(a). Making IrO_2 a good testbed for the switching of properties is also the fact that IrO_2 is a metal with Fermi energy at a half-filled level, without magnetic ordering (except tentatively in ultrathin films [113]) or other phase transitions down to low temperatures. The IrO_2 single-crystal films were grown by MBE with orientations (110), (100), (001), (101), and (111) on single-crystal TiO_2 of corresponding orientations. The Hall effect was measured from 300 K to 2 K with the magnetic field applied normal to the film plane, hence along different crystallographic directions (figure 11(a)). The dominant carrier type indicated by the Hall effect is found to be controlled by the crystallographic direction of the magnetic field, indicating a pronounced anisotropy of the Hall coefficient. Hole contributions dominate for magnetic fields along [100] and [110], and electron contributions along [001] and [101], while [111] shows nearly compensated behavior, consistent over the range of measurement temperatures (figure 11(b)). First-principles calculations of the band structure complemented by Boltzmann transport theory show that the observed dependence of dominant carrier type on magnetic field direction has its origin in the anisotropic and non-trivial electronic structure and Fermi surface of the nonsymmorphic IrO_2. The nonsymmorphic structure of IrO_2 hence allows a unique switching of carrier type based on the magnetic field direction, a phenomenon of potential use in electronics applications.

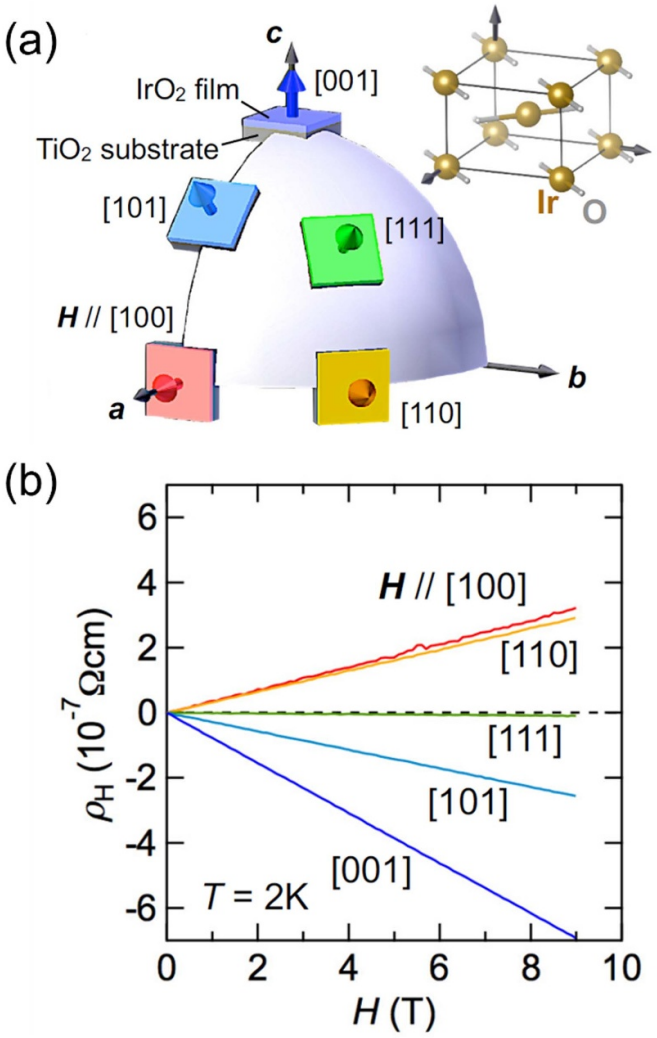

Figure 11. Measurements of the Hall resistivity obtained with magnetic fields along different crystallographic directions of IrO_2 indicate different carrier types (electron or hole). (a) A sketch of the magnetic field directions and film orientations for the Hall resistivity measurements, with the IrO_2 rutile structure shown in the same orientation. (b) The Hall resistivity vs magnetic field obtained at 2 K for different magnetic field orientations. The measurements indicate hole contributions in the [100] and [110] orientations, electron contributions in [001] or [101], and compensated behavior in [111]. Reprinted (figure) with permission from [126], Copyright (2015) by the American Physical Society.

4.1.3. Nanowire electrical transport properties. Spurred by progress in 1D nanostructure synthesis methods, recent studies have turned to electronic properties of IrO_2 nanorod/nanowires, where rich phenomena and unanticipated quantum

states that rely on the existence of the DNL, strong SOC, and controlled disorder and doping have been uncovered.

While studying single-crystal IrO_2 nanorods, Lin *et al* [199, 200] observed a metallic behavior from 300 K to 50 K, with a weak upturn in resistivity with decreasing T below 50 K. Such an upturn is in fact regularly observed in IrO_2 of lower dimensionality (wires and thin films). The nanorods show a substantially higher resistivity over the range of T compared to bulk IrO_2 (at 300 K about 270 mΩ cm compared to 85 mΩ cm), and also show residual resistivity ratios (300 K resistivity/4 K resistivity) of only ∼1.2, compared to ∼500 for bulk crystals [98]. Both observations point to a high level of point defects. An analysis of resistivity vs T shows that the T-dependent part of the resistivity is due to standard acoustic and optical phonon scattering, with $\theta_D \approx 315$ K, similar to $\theta_D \approx 290$ K found in bulk crystals [98].

As an example of an uncommon quantum state observation, Yeh *et al* [201] investigated the transport properties of IrO_2 (and RuO_2) nanowires as a function of T (figure 12), where they found the crystal symmetries that enforce the DNL of IrO_2 also give rise to nonmagnetic Kondo correlations. The O vacancies in the IrO_2 nanowires drive an orbital two-channel Kondo effect, where the degree of freedom is a pseudospin from orbital degrees of freedom. The near-degeneracy of the Ir d_{xz} and d_{yz} orbitals near an O vacancy is due to symmetry properties of IrO_2 and these orbitals form the pseudospin basis. The two defect electrons from the vacancy act as two independent Kondo screening channels. The O vacancy system can thus support an orbital two-channel Kondo effect. The resistivity of the nanowires drops linearly in $T^{1/2}$ below a characteristic Kondo temperature $T_K \approx 20$ K, as shown in figure 12. The resistivity shows metallic behavior for $T > T_K$. The dependence on T is consistent with the existence of a two-channel Kondo effect. Other origins of the dependence on T, including effects of electron-electron interactions and disorder, are counted as unlikely by the authors. Yeh *et al* [201] hence showed that defect engineering in IrO_2 nanowires can provide unique unconventional non-Fermi-liquid quantum phenomena.

Closer to established mesoscopic quantum coherence effects in metallic nanowires, Chien *et al* [202] and Lin *et al* [203] demonstrated quantum interference effects in IrO_2 nanowires that were annealed in vacuum to generate O vacancies. Noise measurements in electronic transport from 1.7 K to 350 K show an increase in $1/f$ noise for $T < 20$ K due to time-dependent universal conductance fluctuations (UCFs, here TUCFs) generated by scattering off mobile defects in the nanowires. UCFs are a fingerprint of quantum interference in disordered mesoscopic conductors, originating from constructive and destructive interference of quantum-coherent carrier trajectories defined by the spatial defect configuration. In a mesoscopic conductor the resulting conductance fluctuations (versus a parameter such as magnetic field, temperature or time) are not averaged out and appear in the measurements at low T where quantum-coherence survives thermal broadening of energy levels. The mobile defects leading to TUCFs in the IrO_2 nanowires are thought to have the same microscopic origin in O vacancies as the defects leading to the two-channel Kondo effect. The TUCFs were used to quantify the quantum phase coherence length of the carriers, showing a length of 90 nm at 1.7 K and 10 nm at 8 K.

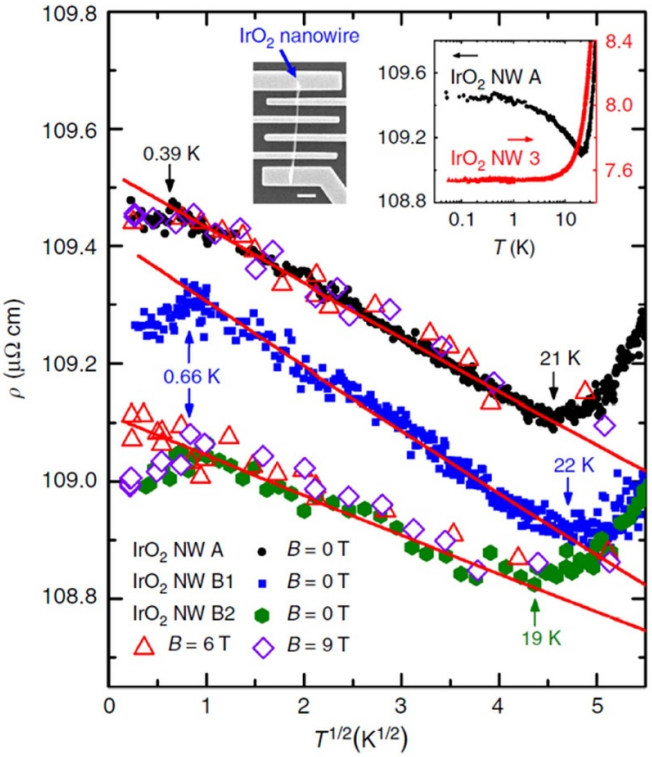

Figure 12. Measurements of resistivity vs T in IrO_2 nanowires indicate a two-channel Kondo effect. The main panel shows the $T^{1/2}$ insulating behavior of resistivity for three nanowires, characteristic of the two-channel Kondo effect. Nanowire (NW) A has a diameter of 130 nm, NW B1 and B2 have 190 nm diameters, while NW 3 is of diameter 330 nm and was oxygenated to have low O vacancy concentration. The left inset (scale bar 1 μm) shows a SEM micrograph of NW A. The right inset shows resistivity vs T in NW A over wider range of T, and in reference metallic NW. Reproduced from [201]. CC BY 4.0.

The presence of both strong SOC and electron correlations can lead to correlated topological states of matter, and searching for these states with an enhancement of electron correlations in IrO_2 is advantageous. An enhancement in electron correlations was noted in vanadium-doped IrO_2 ($Ir_{1-x}V_xO_2$) nanowires [161]. Since strong electron correlations are present in 3*d* TMO VO_2, the enhancement in electron correlations was pursued as a deliberate result of the V-doping, with the aim to increase correlations in the otherwise relatively weakly interacting IrO_2 system. The nanowires in this work had rectangular cross-sections and effective diameters from 87 nm to 149 nm. T-dependent electrical resistivity measurements were carried out to study the effects of V-doping, where the doped nanowires had electrical resistivity orders of magnitude higher than undoped IrO_2 (figure 13(a)). Significantly, the nanowires showed a mild non-metallic upturn in resistivity with decreasing T starting in a certain range of low T (figure 13(b)). Several mechanisms can contribute to the weak upturn in resistivity, including a Kondo effect, localization effects, and corrections due to electron-electron interactions. Analysis of the

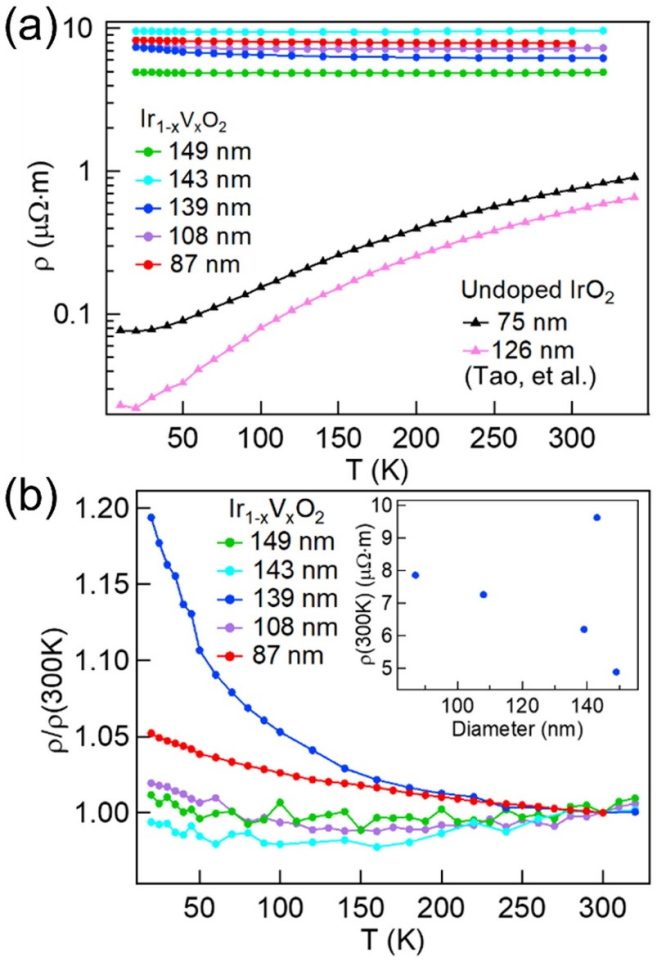

Figure 13. (a) Temperature dependent resistivity of undoped and V-doped IrO_2 nanowires, revealing significantly increased resistivity upon V-doping. The undoped data were originally adapted from [204] in [161]. (b) Resistivity of the V-doped nanowires normalized at 300 K to display its temperature dependence for nanowires with different diameters. The resistivity values at 300 K are shown in the inset. Reproduced from [161]. CC BY 4.0.

resistivity vs T shows that in this doped disordered system, both an orbital two-channel Kondo effect and the resistivity correction from electron–electron interactions can account for the observations, with no ready means of distinguishing their contributions individually. It is noted that both mechanisms rely on strengthened electron correlations, and that the V-doping succeeded in enhancing electron correlations in the IrO_2 nanowires [161].

The above examples demonstrate that in nanowire form, the tunability of the IrO_2 electronic properties can be fully exploited in the search for new quantum phenomena and states of matter. Future experiments and theoretical developments have a fruitful path to follow up on the initial studies.

4.2. Spin transport

The strong SOC in IrO_2 leads to a large spin Hall angle, which makes the material attractive in spintronics for charge-to-spin conversion (spin Hall effect, for spin-current generation) or spin-to-charge conversion (inverse spin Hall effect, for spin-current detection). To date, studies have confirmed large spin Hall angles θ_{SH}, of which the sign and magnitude however vary with crystallinity and preferential surface or interface texture ((100), (110), etc) and can depend on T. The variation and dependence on T are attributed to different intrinsic SOC mechanisms and different spin-dependent scattering mechanisms (skew scattering, side jump mechanism) prevailing depending on conditions. The studies so far clearly indicate that controlling the surfaces and interfaces is necessary for use of IrO_2 in spintronics applications.

The pioneering work by Fujiwara *et al* [51] studied the inverse spin Hall effect in amorphous and polycrystalline IrO_2 thin films using a nonlocal spin valve geometry in the shape of a triple cross bar, with Ag as spin transport bar, two permalloy cross bars as spin-current injection electrodes, and an IrO_2 cross bar for spin-current detection by the inverse spin Hall effect (figures 14(a) and (b)). Inverse Hall effect was clearly observed in both the polycrystalline and amorphous samples (figures 14(c) and (d)). At 300 K, the spin Hall angles are found to be: $\theta_{SH} = 0.040$ for the polycrystalline IrO_2 and $\theta_{SH} = 0.065$ for the amorphous IrO_2. These values are comparable to θ_{SH} in Pt, Pd, β-W, β-Ta, and other metals often used for spin-current detection (figure 14(e)). Moreover, the inverse spin Hall voltage is proportional to the product of θ_{SH} with electrical resistivity (the product is the spin Hall resistivity, which determines the efficiency of spin-current detection). The relatively higher resistivity of IrO_2 compared to elemental metals creates an additional advantage for spin-current detection. The work also found that the Ag/IrO_2 interface is well-defined. The θ_{SH} changes sign at $T = 90$ K ($\theta_{SH} > 0$ above 90 K to $\theta_{SH} < 0$ below 90 K), which was ascribed to the coexistence of different SOC mechanisms yielding different signs. While a large θ_{SH} is a promising hallmark in IrO_2 thin films, the complexities introduced by competing SOC mechanisms and a sensitivity to film orientation, morphology and strain have also been emphasized in subsequent work, as discussed below.

Various experimental approaches have recently been applied to obtain values for θ_{SH}. These include measurements on spin valves, ferromagnetic resonance (FMR), and measurements of the spin Seebeck effect, with examples reviewed below. The spin Hall conductivity and θ_{SH} were studied by Bose *et al* [205] in single-crystalline IrO_2 (001) and (110) thin films, with results shown in figure 15. The measurements occurred by spin-torque FMR to obtain an effective spin Hall conductivity. For (001) IrO_2, the spin Hall angles are determined to be $\theta_{SH} = 0.45$ at 300 K and $\theta_{SH} = 0.65$ at 30 K, among the highest θ_{SH} measured on IrO_2 (figure 15) [140, 141] and of opposite sign to some other results [124]. In (110) films, θ_{SH} is much reduced and is anisotropic for different current directions; both effects ascribed to anisotropic strain in the (110) films contrasted with the isotropic strain in the (001) films (figure 15). The contributions to the spin Hall conductivity near the DNLs are indeed expected to be very sensitive to strain. The work demonstrates the tunability and effect of orientation and strain on the spin Hall effect in IrO_2.

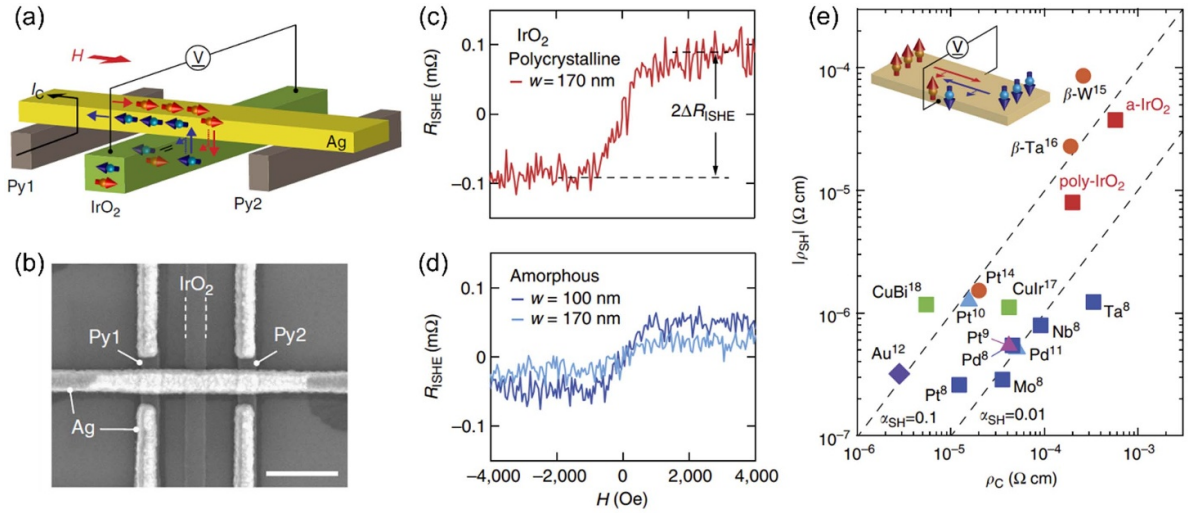

Figure 14. The lateral nonlocal spin-valve geometry used in [51] to study the inverse spin Hall effect via the spin Hall resistivity and spin Hall angle. (a) The spin-valve geometry has the shape of a triple cross bar, with a Ag spin transport bar, two permalloy cross bars as spin-injection electrodes, and an IrO_2 cross bar for spin-current detection by the inverse spin Hall effect. The spin Hall angles obtained in [51] are comparable to those measured in other metals often used for spin-current detection. (b) A SEM micrograph of a typical spin-valve, with scale bar of 500 nm. The dotted lines indicate the edges of the IrO_2 wire. The inverse spin Hall resistance versus magnetic field measured on (c) a polycrystalline wire and (d) an amorphous wire. (e) A summary of measured spin Hall resistivity ρ_{SH} and electric resistivity ρ_c for different metals, which shows considerably large ρ_{SH} in IrO_2 compared with some typical heavy metals and alloys. Reproduced from [51], with permission from Springer Nature.

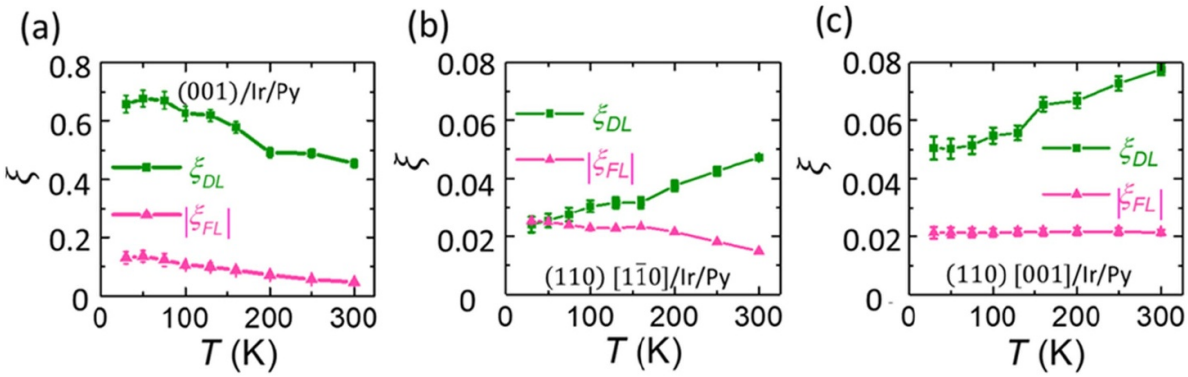

Figure 15. Spin Hall angles vs T, measured on thin film IrO_2 via spin-torque ferromagnetic resonance in [12]. The spin Hall angles are the damping-like ξ_{DL} and the field-like ξ_{FL} as measured from the spin torques, where ξ_{DL} is of relevance for comparisons of the spin Hall resistivity in materials. (a) Spin Hall angles for (001) IrO_2, showing large values of 0.45 at 300 K and 0.65 at 30 K, among the highest measured on IrO_2. (b)–(c) Spin Hall angles for anisotropically strained (110) IrO_2, showing much reduced and anisotropic values. Reprinted with permission from [205]. Copyright (2020) American Chemical Society.

Deeper understanding of SOC mechanisms in IrO_2 is desired for better control of spin-to-charge conversion in the material [206], as illustrated by the varying sign and magnitudes for θ_{SH} reported so far. To illustrate, Jiménez–Cavero *et al* [124] studied θ_{SH} in polycrystalline Fe_2O_3/IrO_2 bilayers using the spin Seebeck effect for the measurements, where they found θ_{SH} is negative and is scaling proportionally to the film resistivity throughout the range of T (50 K–300 K) and of thickness (2 nm–22 nm). Several mechanisms contributing to the spin Hall effect were discussed, including skew scattering, the side jump mechanism and the intrinsic SOC mechanism, and conclude that, in their work, the likely dominant contribution arises from the intrinsic SOC mechanism. Because one mechanism dominates, the sign of θ_{SH} remains consistent. The results indicate that crystallinity and preferential texture (here (100)) can be used to control the sign and magnitude of the inverse spin Hall effect and that low θ_{SH} values in the literature may be due to coexisting and competing mechanisms in one given sample leading to different signs.

In conventional spin-orbit torques (SOTs), the spin polarization directions generating the torque on magnetization are constrained to be orthogonal to both spin-current and charge-current directions, limiting magnetization switching to just one direction. While lower-symmetry materials offer more choices for the spin polarization, high-symmetry IrO_2 can be used with surfaces having lower-symmetry orientations, like (110) or (111), and with lower-symmetry crystallographic directions for applied current. The lower-symmetry surfaces and current

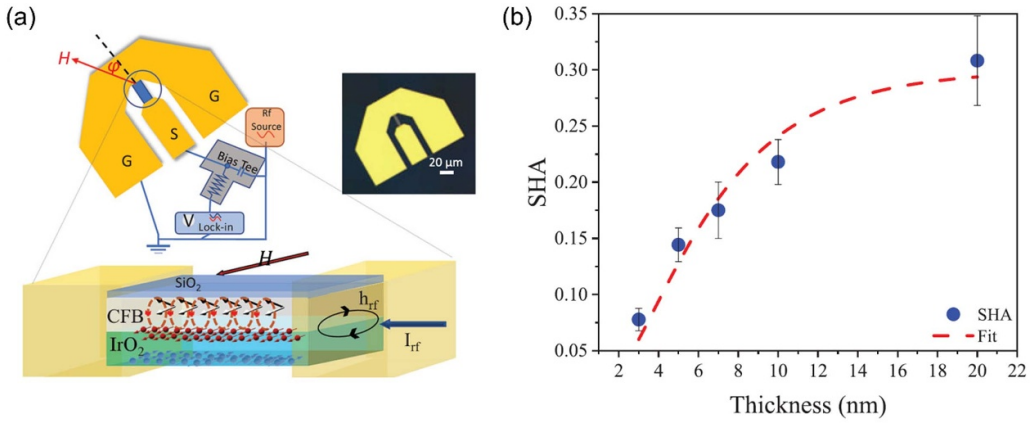

Figure 16. (a) A schematic of the spin-torque ferromagnetic resonance setup and a picture of the IrO_2/CoFeB bilayer samples used in [16] to measure spin-charge conversion in polycrystalline thin films of IrO_2. (b) The spin Hall angles measured at room temperature vs IrO_2 thickness. Tokura and Nagaosa [16] finds spin Hall angles up to 0.31 in the polycrystalline IrO_2, about 4x larger than that found in Pt in comparable Pt/CoFeB bilayers. Reprinted from [141], with the permission of AIP Publishing.

directions form a route for breaking the constraints inherent in conventional SOTs. IrO_2 has formed the basis for a search for such unconventional SOTs in [142], where spin-currents with unconventional spin polarizations can then be produced. The work studied the spin Hall effect in (001), (110), and (111) oriented films along different in-plane crystallographic directions using spin-torque FMR. The films were grown on TiO_2 via RF magnetron sputtering with a permalloy overlayer used as spin detector.

Examples of the various magnitudes and signs for spin-to-charge conversion in IrO_2 observed in the growing literature are discussed below [207], in conjunction with the nature of the films and the measurement method, both of which may play a role in the results. Sahoo *et al* [140] applied FMR spin pumping in IrO_2/CoFeB bilayers (figure 16) to study inverse spin Hall voltages. Polycrystalline IrO_2 was obtained in the bilayer, through DC magnetron sputtering on Si (100). Spin pumping transfers spin angular momentum from a ferromagnet (CoFeB) to an adjacent nonmagnetic material (IrO_2) under an external magnetic field and a microwave excitation field, and the inverse spin Hall effect converts the spin-current to charge-current for measurements. Damping of the FMR signal was also used for measurements. The results show high $\theta_{SH} = 0.26$ in the polycrystalline IrO_2 at 300 K, comparable to results of [205]. Using similar approaches Sahoo *et al* [141] reported large θ_{SH} in polycrystalline IrO_2/CoFeB bilayers using spin-torque FMR experiments, linewidth modulation experiments and line shape analysis, with the setup and typical sample depicted in figure 16. The films were vacuum-annealed, resulting in improved intergrain conductance and lower roughness. The spin Hall angle is $\theta_{SH} = 0.31$ in the optimized polycrystalline IrO_2 (figure 16), which is about 4x larger than that found in Pt in a comparable Pt/CoFeB bilayer studied in parallel ($\theta_{SH} = 0.07$). The improved conductivity and low roughness in the optimized polycrystalline films likely contributed to the high $\theta_{SH} = 0.31$, which is comparable to the crystalline film result in [205]. Using spin-torque generation in permalloy ($Ni_{81}Fe_{19}$)/IrO_2 bilayers and measuring second-harmonic Hall resistance, Ueda *et al* [143] reported an effective $\theta_{SH} = +0.093 \pm 0.003$ and a spin-diffusion length $= 1.7 \pm 0.2$ nm at 300 K. The work again shows that θ_{SH} in IrO_2 is comparable to that in Pt and in fact 7x higher than that in elemental Ir. Furthermore, the same group studied a stacking-order effect, where the magnetic and spin-transport properties for two distinct stacking configurations, i.e. substrate/TaO_x/$Ni_{81}Fe_{19}$/IrO_2 (IrO_2-T) and substrate/IrO_2/$Ni_{81}Fe_{19}$/ TaO_x (IrO_2-B), were compared [144]. The IrO_2-B sample possesses a positive sign for the field-like SOT, whereas a negative sign was observed in the IrO_2-T sample which was attributed to the oxidation of the $Ni_{81}Fe_{19}$ at the $Ni_{81}Fe_{19}$/IrO_2 interface. Since O_2 gas was introduced in the deposition of IrO_2, the surface oxidation of $Ni_{81}Fe_{19}$ was more significant in the IrO_2-T sample than in the IrO_2-B. The oxidation possibly enhances the interface Rashba–Edelstein effect, yielding a negative sign in the field-like SOT [208–212]. The damping-like SOT is positive for both samples, but its magnitude is lower in the IrO_2-T sample than in the IrO_2-B sample, possibly due to an intermixing effect which reduces the spin transparency at the interface [213–215].

Qiu *et al* deposited IrO_2 film on a $Y_3Fe_5O_{12}$ (YIG) film to form an all-oxide spintronics device for the observation of the spin Seebeck effect in the IrO_2 [216]. All-oxide spintronics devices, in many cases, have promising applications where optical transparency is required. IrO_2 with its high θ_{SH} is an attractive component in this quest. In the experiments, via the spin Seebeck effect, a temperature gradient maintained across the YIG/IrO_2 interface injects a spin current into the IrO_2 which is then detected by the inverse spin Hall voltage over contacts on the IrO_2. The small magnitude of the measured inverse spin Hall voltage indicates a small spin-mixing conductance at this particular YIG/IrO_2 interface. Realization of all-oxide spin Seebeck devices hence requires engineering of the oxide interface for optimum spin-mixing conductance, which can be achieved by interlayers, annealing, or doping.

4.3. Thermal transport

Like many other TMOs, the thermal transport properties of IrO_2 have been far less studied than their electrical and spin transport properties. This may be due to the conventional wisdom that TMOs have relatively low thermoelectric figure of merit in comparison to other families of materials such as metal chalcogenides. The thermal transport of IrO_2, however, is of particular interest for fundamental research owing to its unique material properties, including the large atomic mass difference between the light oxygen and heavy iridium atoms, the strong interatomic bonding, the relatively complex crystal structure that contains six atoms in a unit cell, as well as the possible interactions between electrons and phonons.

The first thermal transport measurement was performed by Tao *et al* [204] on single crystalline IrO_2 nanowires grown by the vapor phase method. Figure 17(a) shows a SEM image of a representative IrO_2 nanodevice for thermal measurement using a standard micro-thermal bridge method [161, 204, 217–219]. The IrO_2 nanowire was positioned between two suspended membranes in proximity which have embedded serpentine platinum coils. Each of the coils was connected electrically to four contact pads for both joule heating and four-terminal resistance measurement. One coil was used as a resistance heater and the other as a resistance thermometer. Pt/C composites were typically deposited at the contacts of the nanowire to minimize the contact thermal resistance. In a typical measurement, a DC voltage was applied to the heater to heat one side of the nanowire by Joule heating. Part of the heat was conducted to the resistance thermometer through the nanowire and increased its temperature. The thermal conductance of the nanowire was derived by solving 1D heat transport equations.

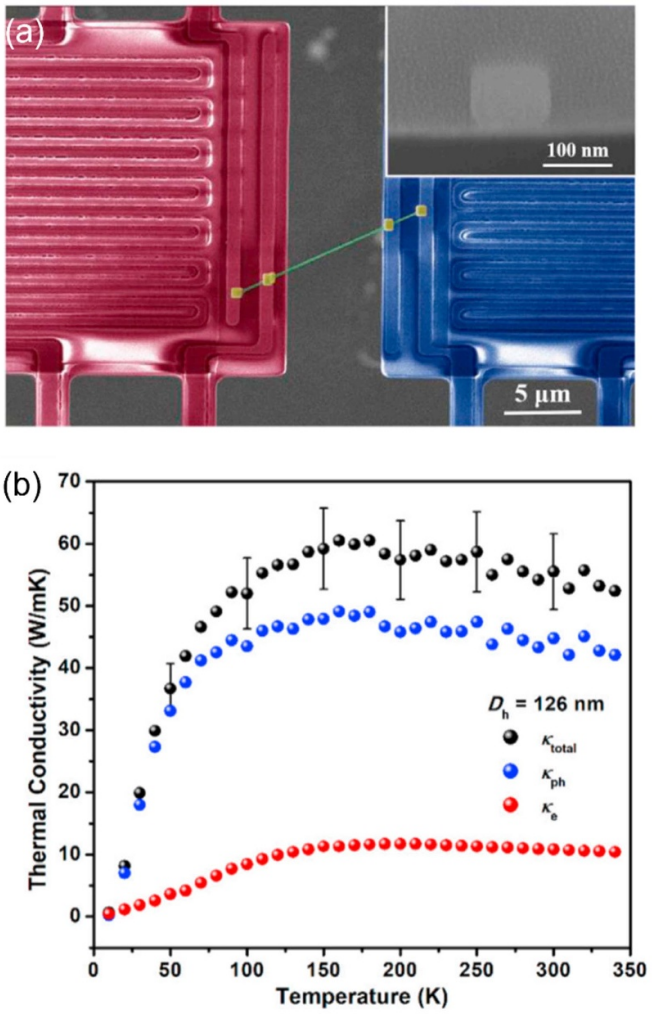

Figure 17. (a) A false-colored SEM image showing a top view of an IrO_2 nanowire device for thermal transport measurement using a micro-thermal bridge method. The nanowire is denoted by the green color. Red and blue indicate the platinum coils embedded in suspended membranes as resistance heater and thermometer, respectively. The inset is an SEM image showing the cross-sectional shape of the nanowire (with the e-beam tilted away from the nanowire axis). The total thermal conductivity κ_{total}, phonon thermal conductivity κ_{ph} and electronic thermal conductivity κ_e of two IrO_2 nanowires with a diameter of 126 nm. Reprinted from [204], Copyright (2021), with permission.

The thermal conductivity of a material is composed of two terms, the electronic thermal conductivity (κ_e) and the lattice/phonon thermal conductivity (κ_{ph}). The κ_e is related to the electrical conductivity σ_e, as described by the Wiedemann–Franz law: $\kappa_e = LT\sigma_e$, where L is the Lorentz number and T is the temperature. Because of the high electrical conductivity of IrO_2, the electrons have a notable (∼20%) contribution to the κ_{tot} (figure 17(b)). The dominant contribution (80%), however, is from phonon transport, differing from many other metals. The high phonon thermal conductivity κ_{ph} is unexpected as each unit cell of IrO_2 contains 6 atoms, corresponding to 15 optical phonon branches, which would promote three-phonon scattering and lead to a low κ_{ph}.

Theoretical studies based on DFT calculations and Boltzmann transport suggest that the high phonon thermal conductivity κ_{ph} is due to two remarkable characteristics of IrO_2. First, the atomic mass of Ir is 12 times as large as that of the O atom; this large atomic mass difference leads to a sizable band gap (between 11 THz and 16 THz) in the phonon dispersion (figure 18(a)). As a result, the Umklapp scattering involving high energy optical branches is significantly suppressed. Indeed, as shown in figure 18(b), the rate of the Umklapp scattering (which poses resistance to thermal transport) is about an order of magnitude lower than the normal scattering rate. Therefore, the three-phonon scattering process is dominated by the normal scattering which satisfies the conservation of phonon momentum with no influence on the thermal conductivity. Second, the interatomic bonding in IrO_2 is strong, leading to high group velocities for the acoustic phonons. Some of the low energy optical branches also have high phonon group velocities, as shown in figure 18(c). Consequently, the phonon thermal conductivity of IrO_2 is relatively high.

It is worth noting, however, that the theoretically calculated κ_{ph} including only the three-phonon scattering is higher than the experimentally measured values (figure 18(d)). To explain

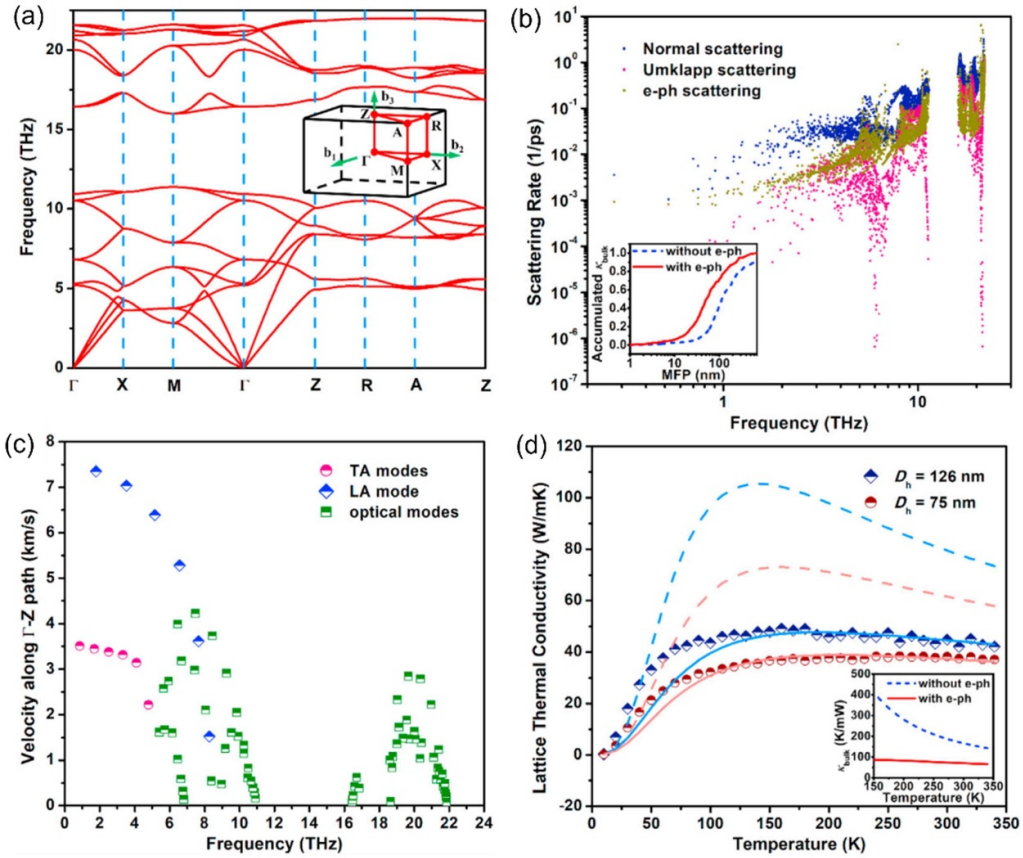

Figure 18. (a) The phonon dispersion of bulk IrO_2 calculated by DFT. (b) A comparison of the calculated scattering rate for normal scattering, Umklapp scattering and electron–phonon (e–ph) scattering. The accumulated thermal conductivity with and without e–ph scattering are compared in the inset. (c) The calculated phonon group velocity for the transverse acoustic (TA) modes, longitudinal acoustic (LA) mode, and optical modes along the $\Gamma - Z$ path. (d) A comparison of the calculated (lines) and measured (dots) κ_{ph} of two nanowires with different diameters. The dashed lines are without considering e–ph scattering, whereas the solid lines are with the e–ph scattering. κ_{ph} of bulk IrO_2 with and without e–ph scattering are shown in the inset. In all cases, a dramatic suppression of κ_{ph} by e–ph scattering is evidenced. Reprinted from [204], Copyright (2021), with permission.

this discrepancy, Tao *et al* [204] added the electron–phonon (e–ph) scattering in their model, where they demonstrated that the e–ph scattering plays an essential role in suppressing the κ_{ph} above ∼50 K[figure 18(d)]. The calculated e–ph scattering rate, shown in figure 18(b), is overall higher than the Umklapp scattering rate. The strong influence of e–ph on thermal conductivity is not often seen in either elemental metals such as Cu, Ag, and Au where three-phonon scattering rate dominates, or semiconductors/insulators which have low conduction electron density and smaller e–ph scattering rate. Furthermore, reduction of κ_{ph} by surface boundary scattering of phonons was also observed both experimentally and theoretically in nanowires with a diameter of ∼100 nm. This suggests that the intrinsic mean free path for phonons is ∼100 nm or longer in bulk IrO_2. The competing effects of the large atomic mass difference and strong inter-atomic bonding against the e–ph scattering and surface boundary scattering gives rise to a relatively high phonon thermal conductivity which is comparable with that of the Si nanowires of a similar diameter [220].

Vanadium doping drastically suppresses the thermal conductivity of the IrO_2 nanowires [161]. As shown in figures 19(a)–(c), both the κ_e and κ_{ph} were reduced by about an order of magnitude at room temperature with 29% vanadium. The reduction of κ_e is related to the suppressed electrical conductivity σ upon doping. At low temperatures, the suppression of κ_{ph} is attributed to the enhanced impurity scattering of phonons by doping, whereas its dramatic decrease at room temperature is due to the enhanced phonon–phonon Umklapp scattering. When some of the Ir atoms are replaced by V, the number of atoms in a primitive unit cell increases and the crystal symmetry is lowered, which gives rise to more complex phonon dispersion (figure 19(d)). Furthermore, since V is lighter than Ir, the atomic mass difference between the metals and oxygen is decreased, yielding a reduction in energy gap between the phonon branches. The increased complexity in the phonon dispersion and the reduction in energy gap collectively enhances the phonon–phonon Umkapp scattering and hence reduces κ_{ph}.

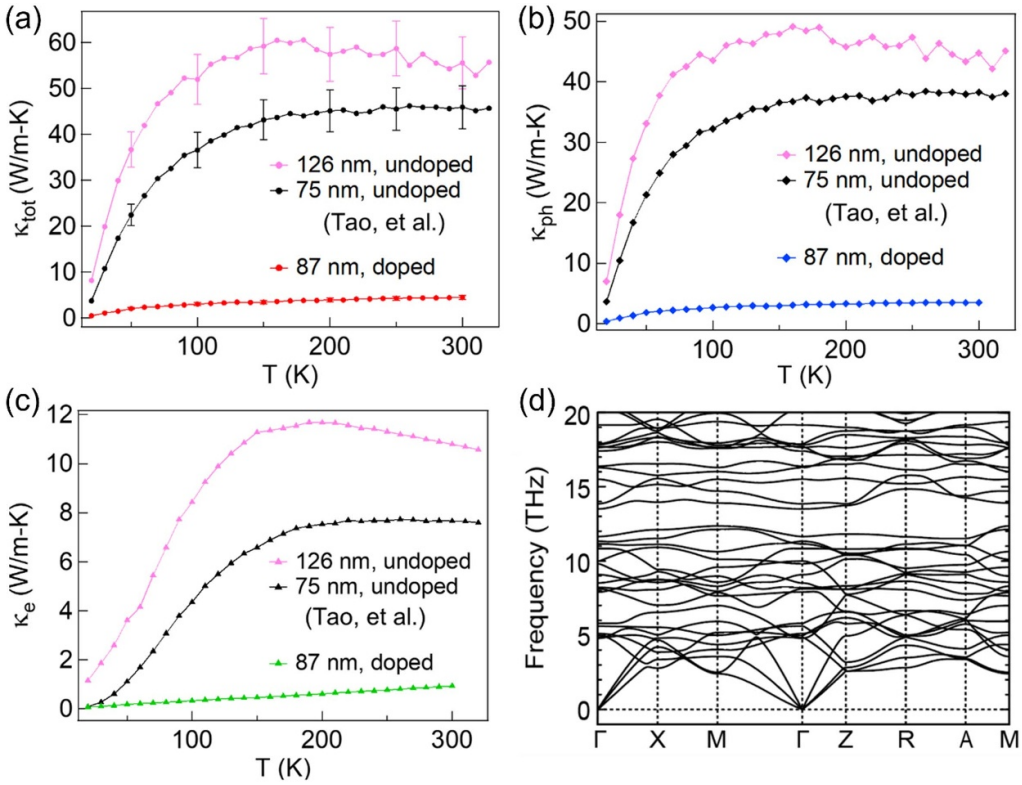

Figure 19. Comparisons of (a) κ_{tot}, (b) κ_{ph}, and (c) κ_e of V-doped and undoped IrO_2 nanowires, which suggests a significant suppression of thermal conductivity by V-doping. The undoped data were originally adapted from [204] in [161]. (d) The calculated phonon dispersion relation of 25% V-doped IrO_2. Reproduced from [161]. CC BY 4.0.

5. Summary and perspectives

In quantum systems, degeneracy as a manifestation of internal symmetry can be observed in experiments. For instance, the paramagnetic nature of molecular oxygen is attributed to the presence of two degenerate antibonding orbitals at the outer shell and to the Hund's rule. Here, in IrO_2, which is a binary oxide with rutile structure, the nonsymmorphic symmetry causes the doubling of degeneracy along *A*–*M* and *X*–*M* directions in the momentum space. Originally, the time-reversal symmetry and inversion symmetry guarantee that every Bloch state is at least doubly degenerate and with the nonsymmorphic symmetry, the fourfold degeneracy is protected along *A*–*M* and *X*–*M*. Thus, it is interesting to wonder whether the fourfold degeneracy can be broken in a realistic system in the presence of, for example, magnetic impurities. IrO_2 is also unique in the sense that the DNLs cross the Fermi level. Therefore, further exploration of the scattering of the corresponding Bloch states with impurities and defects is critical for understanding the spin and/or charge transport properties [221, 222].

Another form of perturbation is the presence of magnetic field, which also breaks the time-reversal symmetry and can be used to map the Fermi surface. The fourfold degeneracy along the *A*–*M* and *X*–*M* directions, has been experimentally verified in IrO_2 with the ARPES [50, 71]. These DNLs occur when the electron-like band is in contact with the hole-like bands around the Fermi level [50]. The richness of such Fermi surfaces may manifest itself through the carrier dynamics in the presence of a weak magnetic field. In a semiclassical picture, carriers are traversing the closed loops inside the Fermi surface in the plane perpendicular to external field [223, 224]. The possibility of carrier tunneling from one electron-like orbit to a hole-like one through the DNL is an interesting question for modeling the carrier dynamics under weak magnetic field.

Experimental study of exotic physical properties strongly relies on the growth of high-quality materials. Bulk crystals, epitaxial thin films, and single-crystalline nanostructures of IrO_2 have been synthesized via a variety of synthetic approaches. Some of these growth techniques (e.g. vapor transport) utilize the high volatile nature of the IrO_3 to realize mass transport for the growth; the high volatility, on the other hand, poses challenges in controlling the stoichiometry of IrO_2 in other deposition processes (e.g. in PLD). Fine tuning of the growth parameters in a coherent way to minimize the loss of Ir and meanwhile to avoid metal dissociation would be essential to those growths. Strain engineering of the oxidation chemistry as used in a recent metal-organic MBE growth [128] is a novel approach to control the formation of competing phases. It would certainly be interesting to study if the same approach is applicable to other growth processes, such as PLD or electron-beam-assisted MBE growth.

Single crystalline nanowires with a sufficiently long length suitable for device fabrication have been realized via vapor transport growth. The diameters of the nanowires are typically on the order of tens of nanometers or larger. It would be of

great interest to achieve ultra-thin wires down to sub-10 nm to explore potentially new transport properties arising from the dimensionality effect. This 1D nanowire growth, however, may not be a trivial task as the IrO_2 nanowires are synthesized via a direct VS mechanism (instead of metal-catalyzed VLS), in which case the wire diameter is less controlled. The anisotropy in the VS growth is strongly influenced by the surface energy difference between facets; therefore, enhancing the surface energy difference by tailoring the growth parameters would be a viable approach to realize 1D ultra-thin wires.

Electronic and magnetotransport properties of IrO_2 have extensively been used as a diagnostic for the numerous phenomena harbored by the bulk crystals, thin to ultrathin films, and nanowires. The richness and tunability of the properties consistently mirror the physics of the competition between the energy scales of SOC, U, and Δ, which yields quantum states depending on strain, doping, dimensionality, film thickness by confinement quantization, temperature, and magnetic field. Apart from the competition, also the presence of DNLs, the strong SOC, and the crystal symmetries bring out unique electronic properties. While from a materials viewpoint IrO_2 appears as a single entity, from the viewpoint of transport properties the material is multifaceted and versatile. Future work should keep the multifaceted nature in mind and analyze electronic transport results accordingly and will undoubtedly add to the list of phenomena hitherto observed. Examples of non-trivial electronic properties include a strong anisotropy of the Hall coefficients, insulating behavior of several possible origins in ultrathin films, and the presence of a rare two-channel Kondo effect in nanowires.

The strong SOC has led to consistent observations of a large spin Hall angle, beneficial in spintronics for spin-current generation and spin-current detection. Future work, particularly regarding control of surfaces and interfaces, will help resolve open questions regarding the sign and magnitude of the spin Hall angle, where variations have been observed. The variations are not entirely surprising given the susceptibility of IrO_2 films to strain, disorder, film thickness, and other parameters. More refined knowledge about the different SOC mechanisms and spin-dependent scattering mechanisms will also contribute to propelling IrO_2 as a prominent spintronics material. Furthermore, the thermal conductivity of IrO_2 turns out to be high among oxides due to the large atomic mass difference between Ir and O, as well as the strong interactomic bonding. The high electrical and thermal conductivities, accompanied by its outstanding spin-based properties, will offer great opportunities for applications in oxide-based electronics and spintronics.

Data availability statement

All data that support the findings of this study are included within the article (and any supplementary files).

Acknowledgments

We thank Professor Ambrose Seo for the helpful discussion. We acknowledge support from the U. S. National Science Foundation through Grants ECCS-1936406 and DMR-2003914, as well as support from the Institute for Advanced Study at Indiana University.

ORCID iDs

A L Coughlin https://orcid.org/0000-0001-9617-9380
Chi-Ken Lu https://orcid.org/0000-0003-1329-6069
J J Heremans https://orcid.org/0000-0002-6346-8597
S X Zhang https://orcid.org/0000-0002-1004-0597

References

[1] Imada M, Fujimori A and Tokura Y M 1998 Insulator transitions *Rev. Mod. Phys.* **70** 1039–263
[2] Salamon M B and Jaime M 2001 The physics of manganites: structure and transport *Rev. Mod. Phys.* **73** 583–628
[3] Yang Z, Ko C and Ramanathan S 2011 Oxide electronics utilizing ultrafast metal-insulator transitions *Annu. Rev. Mater. Res.* **41** 337–67
[4] Bednorz J G and Müller K A 1986 Possible highTc superconductivity in the Ba−La−Cu−O system *Z. Phys.* B **64** 189–93
[5] Wu M K, Ashburn J R, Torng C J, Hor P H, Meng R L, Gao L, Huang Z J, Wang Y Q and Chu C W 1987 Superconductivity at 93 K in a new mixed-phase Y-Ba-Cu-O compound system at ambient pressure *Phys. Rev. Lett.* **58** 908–10
[6] Lee P A, Nagaosa N and Wen X-G 2006 Doping a Mott insulator: physics of high-temperature superconductivity *Rev. Mod. Phys.* **78** 17
[7] Keimer B, Kivelson S A, Norman M R, Uchida S and Zaanen J 2015 From quantum matter to high-temperature superconductivity in copper oxides *Nature* **518** 179–86
[8] von Helmolt R, Wecker J, Holzapfel B, Schultz L and Samwer K 1993 Giant negative magnetoresistance in perovskitelike $La_{2/3}Ba_{1/3}MnO_x$ ferromagnetic films *Phys. Rev. Lett.* **71** 2331–3
[9] Jin S, Tiefel T H, McCormack M, Fastnacht R A, Ramesh R and Chen L H 1994 Thousandfold change in resistivity in magnetoresistive La-Ca-Mn-O films *Science* **264** 413–5
[10] Dagotto E, Hotta T and Moreo A 2001 Colossal magnetoresistant materials: the key role of phase separation *Phys. Rep.* **344** 1–153
[11] Ramirez A 1997 Colossal magnetoresistance *J. Phys.* **9** 8171
[12] Fiebig M, Lottermoser T, Fröhlich D, Goltsev A V and Pisarev R V 2002 Observation of coupled magnetic and electric domains *Nature* **419** 818–20
[13] Zheng H *et al* 2004 Multiferroic $BaTiO_3$-$CoFe_2O_4$ nanostructures *Science* **303** 661–3
[14] Spaldin N A and Ramesh R 2019 Advances in magnetoelectric multiferroics *Nat. Mater.* **18** 203–12
[15] Dagotto E 1994 Correlated electrons in high-temperature superconductors *Rev. Mod. Phys.* **66** 763–840
[16] Tokura Y and Nagaosa N 2000 Orbital physics in transition-metal oxides *Science* **288** 462–8
[17] Hasan M Z and Kane C L 2010 Colloquium: topological insulators *Rev. Mod. Phys.* **82** 3045–67
[18] Qi X-L and Zhang S-C 2011 Topological insulators and superconductors *Rev. Mod. Phys.* **83** 1057–110
[19] Moore J E 2010 The birth of topological insulators *Nature* **464** 194–8
[20] Clancy J P, Chen N, Kim C Y, Chen W F, Plumb K W, Jeon B C, Noh T W and Kim Y-J 2012 Spin-orbit coupling in iridium-based 5_d compounds probed by x-ray absorption spectroscopy *Phys. Rev.* B **86** 195131

[21] Cho D-Y, Park J, Yu J and Park J-G 2012 X-ray absorption spectroscopy studies of spin–orbit coupling in 5d transition metal oxides *J. Phys.* **24** 055503

[22] Witczak-Krempa W, Chen G, Kim Y B and Balents L 2014 Correlated quantum phenomena in the strong spin-orbit regime *Annu. Rev. Condens Matter Phys.* **5** 57–82

[23] Rau J G, Lee E K-H and Kee H-Y 2016 Spin-orbit physics giving rise to novel phases in correlated systems: iridates and related materials *Annu. Rev. Condens. Matter Phys.* **7** 195–221

[24] Schaffer R, Lee E K-H, Yang B-J and Kim Y B 2016 Recent progress on correlated electron systems with strong spin–orbit coupling *Rep. Prog. Phys.* **79** 094504

[25] Kim B J *et al* 2008 Novel $J_{\rm eff}$=1/2 Mott state induced by relativistic spin-orbit coupling in Sr_2 IrO_4 *Phys. Rev. Lett.* **101** 076402

[26] Kim B J, Ohsumi H, Komesu T, Sakai S, Morita T, Takagi H and Arima T 2009 Phase-sensitive observation of a spin-orbital Mott state in Sr_2IrO_4 *Science* **323** 1329–32

[27] Pesin D and Balents L 2010 Mott physics and band topology in materials with strong spin–orbit interaction *Nat. Phys.* **6** 376–81

[28] Wan X, Turner A M, Vishwanath A and Savrasov S Y 2011 Topological semimetal and Fermi-arc surface states in the electronic structure of pyrochlore iridates *Phys. Rev.* B **83** 205101

[29] Kondo T *et al* 2015 Quadratic Fermi node in a 3D strongly correlated semimetal *Nat. Commun.* **6** 10042

[30] Varnava N and Vanderbilt D 2018 Surfaces of axion insulators *Phys. Rev.* B **98** 245117

[31] Chaloupka J, Jackeli G and Khaliullin G 2010 Kitaev-Heisenberg model on a Honeycomb lattice: possible exotic phases in iridium oxides A_2IrO_3 *Phys. Rev. Lett.* **105** 027204

[32] Singh Y, Manni S, Reuther J, Berlijn T, Thomale R, Ku W, Trebst S and Gegenwart P 2012 Relevance of the Heisenberg-Kitaev model for the Honeycomb lattice iridates A_2IrO_3 *Phys. Rev. Lett.* **108** 127203

[33] Dey T, Mahajan A V, Khuntia P, Baenitz M, Koteswararao B and Chou F C 2012 Spin-liquid behavior in $J_{\rm eff}$=1/2 triangular lattice compound $Ba_3IrTi_2O_9$ *Phys. Rev.* B **86** 140405

[34] Takayama T, Kato A, Dinnebier R, Nuss J, Kono H, Veiga L S I, Fabbris G, Haskel D and Takagi H 2015 Hyperhoneycomb iridate $\beta-Li_2IrO_3$ as a platform for Kitaev magnetism *Phys. Rev. Lett.* **114** 077202

[35] Kong D *et al* 2011 Rapid surface oxidation as a source of surface degradation factor for Bi_2Se_3 *ACS Nano* **5** 4698–703

[36] Li Z, Xu E, Losovyj Y, Li N, Chen A, Swartzentruber B, Sinitsyn N, Yoo J, Jia Q and Zhang S 2017 Surface oxidation and thermoelectric properties of indium-doped tin telluride nanowires *Nanoscale* **9** 13014–24

[37] Coughlin A L *et al* 2023 Extreme air sensitivity and nonself-limited oxidation of two-dimensional magnetic tellurides *ACS Mater. Lett.* **5** 1945–53

[38] Sanchez Casalongue H G, Ng M L, Kaya S, Friebel D, Ogasawara H and Nilsson A 2014 In situ observation of surface species on iridium oxide nanoparticles during the oxygen evolution reaction *Angew. Chem., Int. Ed.* **53** 7169–72

[39] Abbott D F, Lebedev D, Waltar K, Povia M, Nachtegaal M, Fabbri E, Copéret C and Schmidt T J 2016 Iridium oxide for the oxygen evolution reaction: correlation between particle size, morphology, and the surface hydroxo layer from operando XAS *Chem. Mater.* **28** 6591–604

[40] Naito T, Shinagawa T, Nishimoto T and Takanabe K 2021 Recent advances in understanding oxygen evolution reaction mechanisms over iridium oxide *Inorg. Chem. Front.* **8** 2900–17

[41] Osterloh F E 2013 Inorganic nanostructures for photoelectrochemical and photocatalytic water splitting *Chem. Soc. Rev.* **42** 2294–320

[42] Butler S R and Gillson J L 1971 Crystal growth, electrical resistivity and lattice parameters of RuO_2 and IrO_2 *Mater. Res. Bull.* **6** 81–89

[43] Kahk J M *et al* 2014 Understanding the electronic structure of IrO_2 using hard-x-ray photoelectron spectroscopy and density-functional theory *Phys. Rev. Lett.* **112** 117601

[44] Kim W J, Kim S Y, Kim C H, Sohn C H, Korneta O B, Chae S C and Noh T W 2016 Spin-orbit coupling induced band structure change and orbital character of epitaxial IrO_2 films *Phys. Rev.* B **93** 045104

[45] Kawasaki J K, Uchida M, Paik H, Schlom D G and Shen K M 2016 Evolution of electronic correlations across the rutile, perovskite, and Ruddelsden-Popper iridates with octahedral connectivity *Phys. Rev.* B **94** 121104

[46] Fang C, Chen Y, Kee H-Y and Fu L 2015 Topological nodal line semimetals with and without spin-orbital coupling *Phys. Rev.* B **92** 081201

[47] Wieder B J, Kim Y, Rappe A M and Kane C L 2016 Double Dirac semimetals in three dimensions *Phys. Rev. Lett.* **116** 186402

[48] Sun Y, Zhang Y, Liu C-X, Felser C and Yan B 2017 Dirac nodal lines and induced spin Hall effect in metallic rutile oxides *Phys. Rev.* B **95** 235104

[49] Li S, Liu Y, Wang S-S, Yu Z-M, Guan S, Sheng X-L, Yao Y and Yang S A 2018 Nonsymmorphic-symmetry-protected hourglass Dirac loop, nodal line, and Dirac point in bulk and monolayer X_3SiTe_6 (X = Ta, Nb) *Phys. Rev.* B **97** 045131

[50] Nelson J N *et al* 2019 Dirac nodal lines protected against spin-orbit interaction in IrO_2 *Phys. Rev. Mater.* **3** 064205

[51] Fujiwara K, Fukuma Y, Matsuno J, Idzuchi H, Niimi Y, Otani Y and Takagi H 2013 5d iridium oxide as a material for spin-current detection *Nat. Commun.* **4** 2893

[52] Kane C L and Mele E J 2005 Quantum spin Hall effect in graphene *Phys. Rev. Lett.* **95** 226801

[53] Sinova J, Valenzuela S O, Wunderlich J, Back C H and Jungwirth T 2015 Spin Hall effects *Rev. Mod. Phys.* **87** 1213–60

[54] Bernevig B A, Hughes T L and Zhang S-C 2006 Quantum spin Hall effect and topological phase transition in HgTe quantum wells *Science* **314** 1757–61

[55] Huang W-D, Cao H, Deb S, Chiao M and Chiao J C 2011 A flexible pH sensor based on the iridium oxide sensing film *Sens. Actuators* A **169** 1–11

[56] Wang C *et al* 2019 Iridium-based catalysts for solid polymer electrolyte electrocatalytic water splitting *ChemSusChem* **12** 1576–90

[57] Jang H and Lee J 2020 Iridium oxide fabrication and application: a review *J. Energy Chem.* **46** 152–72

[58] Chen Z, Duan X, Wei W, Wang S and Ni B-J 2020 Iridium-based nanomaterials for electrochemical water splitting *Nano Energy* **78** 105270

[59] Scarpelli F, Godbert N, Crispini A and Aiello I 2022 Nanostructured iridium oxide: state of the art *Inorganics* **10** 115

[60] Zwartsenberg B *et al* 2020 Spin-orbit-controlled metal–insulator transition in Sr_2IrO_4 *Nat. Phys.* **16** 290–4

[61] Sohn C H *et al* 2013 Mixing between $J_{\rm eff}$=1/2 and 3/2 orbitals in Na_2IrO_3: a spectroscopic and density functional calculation study *Phys. Rev.* B **88** 085125

[62] Katukuri V M, Nishimoto S, Yushankhai V, Stoyanova A, Kandpal H, Choi S, Coldea R, Rousochatzakis I, Hozoi L and Van Den Brink J 2014 Kitaev interactions between j= 1/2 moments in honeycomb Na_2IrO_3 are large and

ferromagnetic: insights from ab initio quantum chemistry calculations *New J. Phys.* **16** 013056
[63] de Almeida J S and Ahuja R 2006 Electronic and optical properties of RuO_2 and IrO_2 *Phys. Rev.* B **73** 165102
[64] Hirata Y, Ohgushi K, Yamaura J-I, Ohsumi H, Takeshita S, Takata M and Arima T-H 2013 Complex orbital state stabilized by strong spin-orbit coupling in a metallic iridium oxide IrO_2 *Phys. Rev.* B **87** 161111
[65] Miao M S and Seshadri R 2012 Rh_2O_3 versus IrO_2: relativistic effects and the stability of Ir^{4+} *J. Phys.* **24** 215503
[66] Ping Y, Galli G and Goddard W A III 2015 Electronic structure of IrO_2: the role of the metal d orbitals *J. Phys. Chem.* C **119** 11570–7
[67] Patil S, Maiti A, Dutta S, Ali K, Mishra P, Pandeya R P, Pramanik A, Datta S, Kandukuri S C and Maiti K 2021 Anomalies in the electronic structure of a 5*d* transition metal oxide, IrO_2 *Phys. Rev. Mater.* **5** 115001
[68] Das P K *et al* 2018 Role of spin-orbit coupling in the electronic structure of IrO_2 *Phys. Rev. Mater.* **2** 065001
[69] Panda S K, Bhowal S, Delin A, Eriksson O and Dasgupta I 2014 Effect of spin orbit coupling and Hubbard *U* on the electronic structure of IrO_2 *Phys. Rev.* B **89** 155102
[70] Mattheiss L F 1976 Electronic structure of RuO_2, OsO_2, and IrO_2 *Phys. Rev.* B **13** 2433–50
[71] Xu X *et al* 2019 Strong spin-orbit coupling and Dirac nodal lines in the three-dimensional electronic structure of metallic rutile IrO_2 *Phys. Rev.* B **99** 195106
[72] Daniels R R, Margaritondo G, Georg C A and Lévy F 1984 Electronic states of rutile dioxides: ruO_2, IrO_2, and $Ru_xIr_{1-x}O_2$ *Phys. Rev.* B **29** 1813–8
[73] Xu J H, Jarlborg T and Freeman A J 1989 Self-consistent band structure of the rutile dioxides NbO_2, RuO_2, and IrO_2 *Phys. Rev.* B **40** 7939–47
[74] Haldane F D M 1988 Model for a quantum Hall Effect without landau levels: condensed-matter realization of the "Parity Anomaly" *Phys. Rev. Lett.* **61** 2015–8
[75] Fu L, Kane C L and Mele E J 2007 Topological insulators in three dimensions *Phys. Rev. Lett.* **98** 106803
[76] Burkov A A, Hook M D and Balents L 2011 Topological nodal semimetals *Phys. Rev.* B **84** 235126
[77] Lu C-K and Herbut I F 2012 Zero modes and charged skyrmions in graphene bilayer *Phys. Rev. Lett.* **108** 266402
[78] Liu C-X, Zhang R-X and VanLeeuwen B K 2014 Topological nonsymmorphic crystalline insulators *Phys. Rev.* B **90** 085304
[79] Chen Y, Kim H-S and Kee H-Y 2016 Topological crystalline semimetals in nonsymmorphic lattices *Phys. Rev.* B **93** 155140
[80] Michel L and Zak J 1999 Connectivity of energy bands in crystals *Phys. Rev.* B **59** 5998–6001
[81] Zhao Y X and Schnyder A P 2016 Nonsymmorphic symmetry-required band crossings in topological semimetals *Phys. Rev.* B **94** 195109
[82] Shiozaki K, Sato M and Gomi K 2016 Topology of nonsymmorphic crystalline insulators and superconductors *Phys. Rev.* B **93** 195413
[83] Lang L-J, Zhang S-L and Zhou Q 2017 Nodal Brillouin-zone boundary from folding a Chern insulator *Phys. Rev.* A **95** 053615
[84] Zhang C, Chen Z Y, Zhang Z and Zhao Y X 2023 General theory of momentum-space nonsymmorphic symmetry *Phys. Rev. Lett.* **130** 256601
[85] Lu C-K and Yip S 2009 Spin current and spin accumulation near a Josephson junction between a singlet and triplet superconductor *Phys. Rev.* B **80** 024504
[86] Carter J-M, Shankar V V, Zeb M A and Kee H-Y 2012 Semimetal and topological insulator in Perovskite iridates *Phys. Rev.* B **85** 115105
[87] Lv B, Qian T and Ding H 2021 Experimental perspective on three-dimensional topological semimetals *Rev. Mod. Phys.* **93** 025002
[88] Xia Y *et al* 2009 Observation of a large-gap topological-insulator class with a single Dirac cone on the surface *Nat. Phys.* **5** 398–402
[89] Chen Y L *et al* 2009 Experimental realization of a three-dimensional topological insulator, Bi_2Te_3 *Science* **325** 178–81
[90] Tanaka Y, Ren Z, Sato T, Nakayama K, Souma S, Takahashi T, Segawa K and Ando Y 2012 Experimental realization of a topological crystalline insulator in SnTe *Nat. Phys.* **8** 800–3
[91] Liu Z K *et al* 2014 Discovery of a three-dimensional topological Dirac semimetal, Na_3Bi *Science* **343** 864–7
[92] Xu S-Y *et al* 2015 Observation of Fermi arc surface states in a topological metal *Science* **347** 294–8
[93] Volovik G E 1992 *Exotic Properties of Superfluid 3He* vol 1 (World Scientific)
[94] Burkov A A and Balents L 2011 Weyl semimetal in a topological insulator multilayer *Phys. Rev. Lett.* **107** 127205
[95] Schmidt P, Binnewies M, Glaum R and Schmidt M 2013 Chemical vapor transport reactions–methods, materials, modeling *Advanced Topics on Crystal Growth* (InTech Rijeka) pp 227–305
[96] Reames F M 1976 Growth of IrO_2, SnO_2, and SnO_2:IrO_2 crystals *Mater. Res. Bull.* **11** 1091–5
[97] Huang Y-S and Liau P-C 1987 Growth and characterization of IrO_2 single crystals *Chin. J. Phys.* **25** 232–42
[98] Lin J J, Huang S M, Lin Y H, Lee T C, Liu H, Zhang X X, Chen R S and Huang Y S 2004 Low temperature electrical transport properties of RuO_2 and IrO_2 single crystals *J. Phys.* **16** 8035
[99] Wertheim G K and Guggenheim H J 1980 Conduction-electron screening in metallic oxides: irO_2 *Phys. Rev.* B **22** 4680–3
[100] Ryden W D, Lawson A W and Sartain C C 1970 Electrical transport properties of IrO_2 and RuO_2 *Phys. Rev.* B **1** 1494–500
[101] Rogers D B, Shannon R D, Sleight A W and Gillson J L 1969 Crystal chemistry of metal dioxides with rutile-related structures *Inorg. Chem.* **8** 841–9
[102] Schäfer H 2013 *Chemical Transport Reactions* (Elsevier) (https://doi.org/10.1016/C2013-0-12396-3)
[103] Triggs P, Georg C and Levy F 1982 Chemical vapour transport of transition-metal oxides (II) epitaxial growth of RuO_2, IrO_2 and (Ru_{1-x}, Ir_x) O_2 on TiO_2 *Mater. Res. Bull.* **17** 671–9
[104] El Khakani M A, Chaker M and Gat E 1996 Pulsed laser deposition of highly conductive iridium oxide thin films *Appl. Phys. Lett.* **69** 2027–9
[105] El Khakani M A and Chaker M 1998 Reactive pulsed laser deposition of iridium oxide thin films *Thin Solid Films* **335** 6–12
[106] El Khakani M A, Drogoff B L and Chaker M 1999 Effect of the deposition temperature on the properties of iridium thin films grown by means of pulsed laser deposition *J. Mater. Res.* **14** 3241–6
[107] Serventi A M, El Khakani M A, Saint-Jacques R G and Rickerby D G 2001 Highly textured nanostructure of pulsed laser deposited IrO_2 thin films as investigated by transmission electron microscopy *J. Mater. Res.* **16** 2336–42
[108] Liu Y, Masumoto H and Goto T 2004 Preparation of IrO_2 thin films by oxidating laser-ablated Ir *Mater. Trans.* **45** 900–3
[109] Liu Y, Masumoto H and Goto T 2004 Electrical and optical properties of IrO_2 thin films prepared by laser-ablation *Mater. Trans.* **45** 3023–7

[110] Zhang L M, Gong Y S, Wang C B, Shen Q and Xia M X 2006 Substrate temperature dependent morphology and resistivity of pulsed laser deposited iridium oxide thin films *Thin Solid Films* **496** 371–5

[111] Gong Y, Wang C, Shen Q and Zhang L 2013 Thermal stability of pulsed laser deposited iridium oxide thin films at low oxygen atmosphere *Appl. Surf. Sci.* **285** 324–30

[112] Bhat S G, Koshy A M, Pittala S and Kumar P S A 2017 Tuning the growth of IrO_2 on $SrTiO_3$ (100) for spin-hall effect based oxide devices *AIP Conf. Proc.* **1859** 020007

[113] Arias-Egido E *et al* 2021 Dimensionality-driven metal–insulator transition in spin–orbit-coupled IrO_2 *Nanoscale* **13** 17125–35

[114] Hou X, Takahashi R, Yamamoto T and Lippmaa M 2017 Microstructure analysis of IrO_2 thin films *J. Cryst. Growth* **462** 24–28

[115] Cordfunke E and Meyer G 1962 The system iridium-oxygen I. measurements on the volatile oxide of iridium *Recl. Trav. Chim. Pays-Bas* **81** 495–504

[116] Yang W C *et al* 2017 Epitaxial thin films of pyrochlore iridate $Bi_{2+x}Ir_{2-y}O_{7-\delta}$: structure, defects and transport properties *Sci. Rep.* **7** 7740

[117] Kim W J, Ko E K, Kim S Y, Kim B and Noh T W 2019 In-operando spectroscopic ellipsometry studies of IrO_2 dynamic instabilities: guide to in-situ growth of pyrochlore iridate thin films *Curr. Appl Phys.* **19** 400–5

[118] Guo L, Shang S-L, Campbell N, Evans P G, Rzchowski M, Liu Z-K and Eom C-B 2021 Searching for a route to synthesize in situ epitaxial $Pr_2Ir_2O_7$ thin films with thermodynamic methods *npj Comput. Mater.* **7** 144

[119] Nishio K, Hwang H Y and Hikita Y 2016 Thermodynamic guiding principles in selective synthesis of strontium iridate Ruddlesden-Popper epitaxial films *APL Mater.* **4** 036102

[120] Liu X, Cao Y, Pal B, Middey S, Kareev M, Choi Y, Shafer P, Haskel D, Arenholz E and Chakhalian J 2017 Synthesis and electronic properties of Ruddlesden-Popper strontium iridate epitaxial thin films stabilized by control of growth kinetics *Phys. Rev. Mater.* **1** 075004

[121] Yang W C *et al* 2018 Stoichiometry control and electronic and transport properties of pyrochlore $Bi_2Ir_2O_7$ thin films *Phys. Rev. Mater.* **2** 114206

[122] Kim W J, Song J, Li Y and Noh T W 2022 Perspective on solid-phase epitaxy as a method for searching novel topological phases in pyrochlore iridate thin films *APL Mater.* **10** 080901

[123] Koshy A M, Bhat S G and Kumar P 2016 Controlled tuning of thin film deposition of IrO_2 on Si using pulsed laser ablation technique *AIP Conf. Proc.* **1728**, 020367

[124] Jiménez-Cavero P, Lucas I, Ara-Arteaga J, Ibarra M R, Algarabel P A and Morellón L 2021 Strong crystallographic influence on spin Hall mechanism in PLD-grown IrO_2 thin films *Nanomaterials* **11** 1478

[125] Kawasaki J K, Kim C H, Nelson J N, Crisp S, Zollner C J, Biegenwald E, Heron J T, Fennie C J, Schlom D G and Shen K M 2018 Engineering carrier effective masses in ultrathin quantum wells of IrO_2 *Phys. Rev. Lett.* **121** 176802

[126] Uchida M, Sano W, Takahashi K S, Koretsune T, Kozuka Y, Arita R, Tokura Y and Kawasaki M 2015 Field-direction control of the type of charge carriers in nonsymmorphic IrO_2 *Phys. Rev.* B **91** 241119

[127] Kawasaki J K, Baek D, Paik H, Nair H P, Kourkoutis L F, Schlom D G and Shen K M 2018 Rutile IrO_2TiO_2 superlattices: a hyperconnected analog to the Ruddelsden-Popper structure *Phys. Rev. Mater.* **2** 054206

[128] Nair S *et al* 2023 Engineering metal oxidation using epitaxial strain *Nat. Nanotechnol.* **18** 1005–11

[129] Beni G, Schiavone L M, Shay J L, Dautremont-Smith W C and Schneider B S 1979 Electrocatalytic oxygen evolution on reactively sputtered electrochromic iridium oxide films *Nature* **282** 281–3

[130] Hackwood S, Schiavone L M, Dautremont-Smith W C and Beni G 1981 Anodic evolution of oxygen on sputtered iridium oxide films *J. Electrochem. Soc.* **128** 2569

[131] Dautremont-Smith W C 1982 Transition metal oxide electrochromic materials and displays: a review: part 2: oxides with anodic coloration *Displays* **3** 67–80

[132] Kreider K 1986 *IrO_2 Radio Frequency Sputtered Thin Film Properties* (American Vacuum Society) (https://doi.org/10.1116/1.573858)

[133] Głab S, Hulanicki A, Edwall G and Ingman F 1989 Metal-metal oxide and metal oxide electrodes as pH sensors *Crit. Rev. Anal. Chem.* **21** 29–47

[134] Liao P C, Ho W S, Huang Y S and Tiong K K 1998 Characterization of sputtered iridium dioxide thin films *J. Mater. Res.* **13** 1318–26

[135] Pinnow C U *et al* 2002 Influence of deposition conditions on Ir/IrO_2 oxygen barrier effectiveness *J. Appl. Phys.* **91** 9591–7

[136] Ishikawa T, Abe Y, Kawamura M and Sasaki K 2003 Formation process and electrical property of IrO_2 thin films prepared by reactive sputtering *Jpn. J. Appl. Phys.* **42** 213

[137] Potrepka D M, Rivas M, Yu H, Polcawich R G, Aindow M and Fox G R 2017 Characterization of IrO_x sputtering for IrO_2 and IrO_2/Pt bottom-electrode piezoelectric micro-electro-mechanical systems applications *Thin Solid Films* **638** 127–37

[138] Choi W S, Seo S S A, Kim K W, Noh T W, Kim M Y and Shin S 2006 Dielectric constants of Ir, Ru, Pt, and IrO_2: contributions from bound charges *Phys. Rev.* B **74** 205117

[139] Cui Y *et al* 2023 In-plane Hall effect in rutile oxide films induced by the Lorentz force (arXiv:2308.06651)

[140] Sahoo B, Roy K, Gupta P, Mishra A, Satpati B, Singh B B and Bedanta S 2021 Spin pumping and inverse spin Hall effect in iridium oxide *Adv. Quantum Technol.* **4** 2000146

[141] Sahoo B, Frano A and Fullerton E E 2023 Efficient charge to spin conversion in iridium oxide thin films *Appl. Phys. Lett.* **123** 032404

[142] Patton M *et al* 2023 Symmetry control of unconventional spin–orbit torques in IrO_2 *Adv. Mater.* **35** 2301608

[143] Ueda K, Moriuchi N, Fukushima K, Kida T, Hagiwara M and Matsuno J 2020 Spin-orbit torque generation in $NiFeIrO_2$ bilayers *Phys. Rev.* B **102** 134432

[144] Ueda K, Moriuchi N, Fukushima K, Kida T, Hagiwara M and Matsuno J 2021 Stacking-order effect on spin-orbit torque, spin Hall magnetoresistance, and magnetic anisotropy in $Ni_{81}Fe_{19}$–IrO_2 Bilayers *Phys. Rev. Appl.* **16** 034039

[145] Arias-Egido E, Laguna-Marco M A, Piquer C, Boada R and Díaz-Moreno S 2019 Toward the optimized spintronic response of Sn-doped IrO_2 thin films *Adv. Funct. Mater.* **29** 1806754

[146] Laguna–Marco M A, Herrero-Albillos J, Aguirre M H, Rueda-Jiménez M and Mikulska I 2023 Novel $Ir_{1-x}Co_xO_2$ thin films: growth and characterization *J. Alloys Compd.* **968** 171975

[147] Arias-Egido E, Laguna-Marco M A, Piquer C, Chaboy J, Fabbris G and Haskel D 2020 Growth and characterization of novel $Ir_{1-x}Cr_xO_2$ thin films *Mater. Des.* **196** 109083

[148] Chen R S, Chen Y S, Huang Y S, Chen Y L, Chi Y, Liu C S, Tiong K K and Carty A J 2003 Growth of IrO_2 films and nanorods by means of CVD: an example of compositional and morphological control of nanostructures *Chem. Vap. Depos.* **9** 301–5

[149] Chen R-S, Huang Y-S, Liang Y-M, Tsai D-S, Chi Y and Kai J-J 2003 Growth control and characterization of

vertically aligned IrO_2 nanorods *J. Mater. Chem.* **13** 2525–9
[150] Chen R-S, Chang H-M, Huang Y-S, Tsai D-S and Chiu K-C 2004 Morphological evolution of the self-assembled IrO2 one-dimensional nanocrystals. *Nanotechnology* **16** 93
[151] Chen R-S, Huang Y-S, Liang Y-M, Hsieh C-S, Tsai D-S and Tiong K-K 2004 Field emission from vertically aligned conductive IrO_2 nanorods *Appl. Phys. Lett.* **84** 1552–4
[152] Wang G, Tsai D-S, Huang Y-S, Korotcov A, Yeh W-C and Susanti D 2006 Selective growth of IrO_2 nanorods using metalorganic chemical vapor deposition *J. Mater. Chem.* **16** 780–6
[153] Chen R-S, Huang Y-S, Tsai D-S, Chattopadhyay S, Wu C-T, Lan Z-H and Chen K-H 2004 Growth of well aligned IrO_2 nanotubes on $LiTaO_3$(012) substrate *Chem. Mater.* **16** 2457–62
[154] Zhang F, Barrowcliff R, Stecker G, Pan W, Wang D and Hsu S-T 2005 Synthesis of metallic iridium oxide nanowires via metal organic chemical vapor deposition *Jpn. J. Appl. Phys.* **44** L398
[155] Chen R S, Chang H M, Huang Y S, Tsai D S, Chattopadhyay S and Chen K H 2004 Growth and characterization of vertically aligned self-assembled IrO_2 nanotubes on oxide substrates *J. Cryst. Growth* **271** 105–12
[156] Wagner R S and Ellis W C 2004 Vapor-liquid-solid mechanism of single crystal growth *Appl. Phys. Lett.* **4** 89–90
[157] Novell-Leruth G, Carchini G and López N 2013 On the properties of binary rutile MO_2 compounds, M = Ir, Ru, Sn, and Ti: a DFT study *J. Chem. Phys.* **138** 194706
[158] Lee Y, Kang M, Shim J H, Lee N-S, Baik J M, Lee Y, Lee C and Kim M H 2012 Growth of highly single crystalline IrO_2 nanowires and their electrochemical applications *J. Phys. Chem.* C **116** 18550–6
[159] Shim J H, Lee Y, Kang M, Lee J, Baik J M, Lee Y, Lee C and Kim M H 2012 Hierarchically driven IrO_2 nanowire electrocatalysts for direct sensing of biomolecules *Anal. Chem.* **84** 3827–32
[160] Zhang T *et al* 2023 Experimental observation of geometric effect on the electron diffraction of quasi-one-dimensional nanostructures *Mater. Today Phys.* **33** 101048
[161] Coughlin A L *et al* 2023 Enhanced electron correlation and significantly suppressed thermal conductivity in Dirac nodal-line metal nanowires by chemical doping *Adv. Sci.* **10** 2204424
[162] Kim I S and Lauhon L J 2012 Increased yield and uniformity of vanadium dioxide nanobeam growth via two-step physical vapor transport process *Cryst. Growth Des.* **12** 1383–7
[163] Lee Y, Shin H-Y, Chun S H, Lee J, Park W J, Baik J M, Yoon S and Kim M H 2012 Highly single crystalline $Ir_xRu_{1-x}O_2$ mixed metal oxide nanowires *J. Phys. Chem.* C **116** 16300–4
[164] Chun S H, Kim H Y, Jang H, Lee Y, Jo A, Lee N-S, Yu H K, Lee Y, Kim M H and Lee C 2017 A facile growth process of highly single crystalline $Ir_{1-x}V_xO_2$ mixed metal oxide nanorods and their electrochemical properties *CrystEngComm* **19** 3455–64
[165] Guiton B S, Gu Q, Prieto A L, Gudiksen M S and Park H 2005 Single-crystalline vanadium dioxide nanowires with rectangular cross sections *J. Am. Chem. Soc.* **127** 498–9
[166] Sohn J I, Joo H J, Porter A E, Choi C-J, Kim K, Kang D J and Welland M E 2007 Direct observation of the structural component of the metal−insulator phase transition and growth habits of epitaxially grown VO_2 nanowires *Nano Lett.* **7** 1570–4
[167] Kim M H *et al* 2009 Growth of metal oxide nanowires from supercooled liquid nanodroplets *Nano Lett.* **9** 4138–46
[168] Chu H, Huang H and Wang J 2017 Clustering on magnesium surfaces—formation and diffusion energies *Sci. Rep.* **7** 5167
[169] Wang J, Huang H and Cale T S 2004 Diffusion barriers on Cu surfaces and near steps *Modelling Simul. Mater. Sci. Eng.* **12** 1209
[170] Huang H and Wang J 2003 Surface kinetics: step-facet barriers *Appl. Phys. Lett.* **83** 4752–4
[171] Holbrough J L, Campbell J M, Meldrum F C and Christenson H K 2012 Topographical control of crystal nucleation *Cryst. Growth Des.* **12** 750–5
[172] Page A J and Sear R P 2009 Crystallization Controlled by the geometry of a surface *J. Am. Chem. Soc.* **131** 17550–1
[173] Tien L-C and Chen Y-J 2012 Effect of surface roughness on nucleation and growth of vanadium pentoxide nanowires *Appl. Surf. Sci.* **258** 3584–8
[174] Cheng C, Liu K, Xiang B, Suh J and Wu J 2012 Ultra-long, free-standing, single-crystalline vanadium dioxide micro/nanowires grown by simple thermal evaporation *Appl. Phys. Lett.* **100**
[175] Yang M-X, Luo W and Chen W 2022 Quantum transport in topological nodal-line semimetals *Adv. Phys.* X **7** 2065216
[176] Li C, Wang C, Wan B, Wan X, Lu H-Z and Xie X 2018 Rules for phase shifts of quantum oscillations in topological nodal-line semimetals *Phys. Rev. Lett.* **120** 146602
[177] Oroszlány L, Dóra B, Cserti J and Cortijo A 2018 Topological and trivial magnetic oscillations in nodal loop semimetals *Phys. Rev.* B **97** 205107
[178] Hu J, Zhu Y, Graf D, Tang Z, Liu J and Mao Z 2017 Quantum oscillation studies of the topological semimetal candidate ZrGe M (M= S, Se, Te) *Phys. Rev.* B **95** 205134
[179] Hu J, Xu S-Y, Ni N and Mao Z 2019 Transport of topological semimetals *Annu. Rev. Mater. Res.* **49** 207–52
[180] Liang T, Gibson Q, Ali M N, Liu M, Cava R and Ong N 2015 Ultrahigh mobility and giant magnetoresistance in the Dirac semimetal Cd_3 As_2 *Nat. Mater.* **14** 280–4
[181] Shekhar C, Nayak A K, Sun Y, Schmidt M, Nicklas M, Leermakers I, Zeitler U, Skourski Y, Wosnitza J and Liu Z 2015 Extremely large magnetoresistance and ultrahigh mobility in the topological Weyl semimetal candidate NbP *Nat. Phys.* **11** 645–9
[182] Gao W, Hao N, Zheng F-W, Ning W, Wu M, Zhu X, Zheng G, Zhang J, Lu J and Zhang H 2017 Extremely large magnetoresistance in a topological semimetal candidate pyrite $PtBi_2$ *Phys. Rev. Lett.* **118** 256601
[183] Wang A, Graf D, Liu Y, Du Q, Zheng J, Lei H and Petrovic C 2017 Large magnetoresistance in the type-II Weyl semimetal WP_2 *Phys. Rev.* B **96** 121107
[184] Hu J, Tang Z, Liu J, Liu X, Zhu Y, Graf D, Myhro K, Tran S, Lau C N and Wei J 2016 Evidence of topological nodal-line fermions in ZrSiSe and ZrSiTe *Phys. Rev. Lett.* **117** 016602
[185] Singha R, Pariari A K, Satpati B and Mandal P 2017 Large nonsaturating magnetoresistance and signature of nondegenerate Dirac nodes in ZrSiS *Proc. Natl Acad. Sci.* **114** 2468–73
[186] Pan H, Tong B, Yu J, Wang J, Fu D, Zhang S, Wu B, Wan X, Zhang C and Wang X 2018 Three-dimensional anisotropic magnetoresistance in the Dirac node-line material ZrSiSe *Sci. Rep.* **8** 9340
[187] Chen W, Lu H-Z and Zilberberg O 2019 Weak localization and antilocalization in nodal-line semimetals: dimensionality and topological effects *Phys. Rev. Lett.* **122** 196603
[188] Zhou T, Tong M, Xie X, Yu Y, Zhu X, Wang Z-Y and Jiang T 2020 Quantum transport signatures of a close candidate

for a type II nodal-line semimetal *J. Phys. Chem. Lett.* **11** 6475–81
[189] Sasmal S, Mondal R, Kulkarni R, Thamizhavel A and Singh B 2020 Magnetotransport properties of noncentrosymmetric CaAgBi single crystal *J. Phys.* **32** 335701
[190] An L, Zhu X, Gao W, Wu M, Ning W and Tian M 2019 Chiral anomaly and nontrivial berry phase in the topological nodal-line semimetal SrA s_3 *Phys. Rev.* B **99** 045143
[191] Laha A, Malick S, Singha R, Mandal P, Rambabu P, Kanchana V and Hossain Z 2019 Magnetotransport properties of the correlated topological nodal-line semimetal YbCdGe *Phys. Rev.* B **99** 241102
[192] Ryden W D, Reed W A and Greiner E S 1972 High-field magnetoresistance of IrO_2 *Phys. Rev.* B **6** 2089–93
[193] Graebner J E, Greiner E S and Ryden W D 1976 Magnetothermal oscillations in RuO_2, OsO_2, and IrO_2 *Phys. Rev.* B **13** 2426–32
[194] Yeh S S, Lin J J, Xiunian J and Dianlin Z 2005 Electron-phonon-impurity interference effect in disordered $Au_{56}Pd_{44}$ and IrO_2 thick films *Phys. Rev.* B **72** 024204
[195] Lin J J, Xu W, Zhong Y L, Huang J H and Huang Y S 1999 Electron-electron scattering times in low-diffusivity thick RuO_2 and IrO_2 films *Phys. Rev.* B **59** 344–8
[196] Egido E A 2020 *Growth and Optimization of Thin Films Based on Iridium Oxide for Spintronics* (Universidad de Zaragoza)
[197] Matsuno J, Ihara K, Yamamura S, Wadati H, Ishii K, Shankar V V, Kee H-Y and Takagi H 2015 Engineering a spin-orbital magnetic insulator by tailoring superlattices *Phys. Rev. Lett.* **114** 247209
[198] Groenendijk D J *et al* 2017 Spin-orbit semimetal $SrIrO_3$ in the two-dimensional limit *Phys. Rev. Lett.* **119** 256403
[199] Lin Y H, Sun Y C, Jian W B, Chang H M, Huang Y S and Lin J J 2008 Electrical transport studies of individual IrO_2 nanorods and their nanorod contacts *Nanotechnology* **19** 045711
[200] Lin Y H, Lee T C, Lin J J, Chang H M and Huang Y S 2006 Electrical measurements on iridium dioxide nanorods *AIP Conf. Proc.* **850** 1484–5
[201] Yeh S-S, Su T-K, Lien A-S, Zamani F, Kroha J, Liao C-C, Kirchner S and Lin J-J 2020 Oxygen vacancy-driven orbital multichannel Kondo effect in Dirac nodal line metals IrO_2 and RuO_2 *Nat. Commun.* **11** 4749
[202] Chien P-Y, Wu C-Y, Wang R-T, Chiu S-P, Kirchner S, Yeh S-S and Lin J-J 2023 Quantum-interference origin and magnitude of 1/f noise in Dirac nodal line IrO_2 nanowires at low temperatures *Appl. Phys. Lett.* **122** 143102
[203] Lin Y-H, Wang L-Y and Lin J-J 2012 Time-dependent universal conductance fluctuations in IrO_2 nanowires *Nanoscale Res. Lett.* **7** 673
[204] Tao Y, Pan Z, Ruch T, Zhan X, Chen Y, Zhang S X and Li D 2021 Remarkable suppression of lattice thermal conductivity by electron-phonon scattering in iridium dioxide nanowires *Mater. Today Phys.* **21** 100517
[205] Bose A, Nelson J N, Zhang X S, Jadaun P, Jain R, Schlom D G, Ralph D C, Muller D A, Shen K M and Buhrman R A 2020 Effects of anisotropic strain on spin–orbit torque produced by the Dirac nodal line semimetal IrO_2 *ACS Appl. Mater. Interfaces* **12** 55411–6
[206] Jadaun P, Register L F and Banerjee S K 2020 Rational design principles for giant spin Hall effect in 5*d*-transition metal oxides *Proc. Natl Acad. Sci.* **117** 11878–86
[207] Chen H and Yi D 2021 Spin–charge conversion in transition metal oxides *APL Mater.* **9** 060908
[208] Akyol M, Alzate J G, Yu G, Upadhyaya P, Wong K L, Ekicibil A, Khalili Amiri P and Wang K L 2015 Effect of the oxide layer on current-induced spin-orbit torques in Hf|CoFeB|MgO and Hf|CoFeB|TaO_x structures *Appl. Phys. Lett.* **106** 032406
[209] Hasegawa K, Hibino Y, Suzuki M, Koyama T and Chiba D 2018 Enhancement of spin-orbit torque by inserting CoO_x layer into Co/Pt interface *Phys. Rev.* B **98** 020405
[210] Xie H, Yuan J, Luo Z, Yang Y and Wu Y 2019 In-situ study of oxygen exposure effect on spin-orbit torque in Pt/Co bilayers in ultrahigh vacuum *Sci. Rep.* **9** 17254
[211] Haney P M, Lee H-W, Lee K-J, Manchon A and Stiles M D 2013 Current induced torques and interfacial spin-orbit coupling: semiclassical modeling *Phys. Rev.* B **87** 174411
[212] Mosendz O, Vlaminck V, Pearson J E, Fradin F Y, Bauer G E W, Bader S D and Hoffmann A 2010 Detection and quantification of inverse spin Hall effect from spin pumping in permalloy/normal metal bilayers *Phys. Rev.* B **82** 214403
[213] Woo S, Mann M, Tan A J, Caretta L and Beach G S D 2014 Enhanced spin-orbit torques in Pt/Co/Ta heterostructures *Appl. Phys. Lett.* **105** 212404
[214] Avci C O, Beach G S D and Gambardella P 2019 Effects of transition metal spacers on spin-orbit torques, spin Hall magnetoresistance, and magnetic anisotropy of Pt/Co bilayers *Phys. Rev.* B **100** 235454
[215] Schuller I K, Kim S and Leighton C 1999 Magnetic superlattices and multilayers *J. Magn. Magn. Mater.* **200** 571–82
[216] Qiu Z, Hou D, Kikkawa T, Uchida K-I and Saitoh E 2015 All-oxide spin Seebeck effects *Appl. Phys. Express* **8** 083001
[217] Kim P, Shi L, Majumdar A and McEuen P L 2001 Thermal transport measurements of individual multiwalled nanotubes *Phys. Rev. Lett.* **87** 215502
[218] Shi L, Li D, Yu C, Jang W, Kim D, Yao Z, Kim P and Majumdar A 2003 Measuring thermal and thermoelectric properties of one-dimensional nanostructures using a microfabricated device *J. Heat Transfer* **125** 881–8
[219] Wingert M C, Chen Z C Y, Kwon S, Xiang J and Chen R 2012 Ultra-sensitive thermal conductance measurement of one-dimensional nanostructures enhanced by differential bridge *Rev. Sci. Instrum.* **83** 024901
[220] Li D, Wu Y, Kim P, Shi L, Yang P and Majumdar A 2003 Thermal conductivity of individual silicon nanowires *Appl. Phys. Lett.* **83** 2934–6
[221] Chen J H, Jang C, Adam S, Fuhrer M S, Williams E D and Ishigami M 2008 Charged-impurity scattering in graphene *Nat. Phys.* **4** 377–81
[222] Yan J and Fuhrer M S 2011 Correlated charged impurity scattering in graphene *Phys. Rev. Lett.* **107** 206601
[223] Cohen M H and Falicov L M 1961 Magnetic breakdown in crystals *Phys. Rev. Lett.* **7** 231–3
[224] Lu C-K and Fertig H A 2014 Magnetic breakdown in twisted bilayer graphene *Phys. Rev.* B **89** 085408